General Disclaimer

One or more of the Following Statements may affect this Document

- This document has been reproduced from the best copy furnished by the organizational source. It is being released in the interest of making available as much information as possible.

- This document may contain data, which exceeds the sheet parameters. It was furnished in this condition by the organizational source and is the best copy available.

- This document may contain tone-on-tone or color graphs, charts and/or pictures, which have been reproduced in black and white.

- This document is paginated as submitted by the original source.

- Portions of this document are not fully legible due to the historical nature of some of the material. However, it is the best reproduction available from the original submission.

AAE

AERONAUTICAL AND ASTRONAUTICAL ENGINEERING DEPARTMENT

ENGINEERING EXPERIMENT STATION, COLLEGE OF ENGINEERING, UNIVERSITY OF ILLINOIS, URBANA

Aeronautical and Astronautical Engineering Department
University of Illinois Urbana, Illinois

Technical Report AAE 85-4
UILU ENG 85-0504

The Use of a Laser Doppler Velocimeter in a Standard Flammability Tube

by

Roger A. Strehlow and Edward M. Flynn
Aeronautical and Astronautical
Engineering Department
University of Illinois at
Urbana-Champaign

Final Report
NASA NAS-32266C
for the period
January 1981 through May 1982

May 1985

50272-101

REPORT DOCUMENTATION PAGE	1. REPORT NO.	2.	3. Recipient's Accession No

4. Title and Subtitle
The Use of a Laser Doppler Velocimeter in a Standard Flammability Tube

5. Report Date
May 1985

6.

7. Author(s)
Roger A. Strehlow and Edward M. Flynn

8. Performing Organization Rept. No.
AAE 85-4

9. Performing Organization Name and Address
Department of Aeronautical and Astronautical Engineering
University of Illinois
105 Transportation Building
104 S. Mathews Ave.
Urbana, IL 61801

10. Project/Task/Work Unit No

11. Contract(C) or Grant(G) No.
(C) NASA NAS-3-22666
(G)

12. Sponsoring Organization Name and Address
NASA Lewis Research Center
210000 Brookpark Road
Cleveland, OH 44135

13. Type of Report & Period Covered
Final
Jan. 1981 - May 1982

14.

15. Supplementary Notes

16. Abstract (Limit: 200 words) The results of the study reported here have bearing on the use of the Laser Doppler Velocimeter, (LDV), to measure the flow associated with the passage of a flame through a Standard Flammability Limit Tube (SFLT). There are four major results of this study. These are:

1. It has been shown that using standard ray tracing calculations one can predict the displacement of the LDV volume and the fringe rotation within the experimental error of measurement.
2. The flow velocity vector field associated with passage of an upward propagating flame in an SFLT has been determined.
3. It has been determined that the use of a light interruption technique to track particles is not feasible.
4. It has been shown that a 25 mW laser would be adequate for LDV measurements in the Shuttle or Space Lab.

17. Document Analysis a. Descriptors
Combustion, flammability limits, zero gravity

b. Identifiers/Open-Ended Terms

c. COSATI Field/Group

18. Availability Statement
Release unlimited

19. Security Class (This Report)
Unclassified

21. No. of Pages
v + 88

20. Security Class (This Page)
Unclassified

22. Price

TABLE OF CONTENTS

	Nomenclature	i
	Abstract	v
I.	INTRODUCTION AND SYNOPSIS OF LDV THEORY	1
	1.1 Introduction	1
	1.2 The Laser Doppler Velocimeter	3
II.	REFRACTIVE EFFECTS	6
	2.1 Introduction	6
	2.2 Deflection Calculations	7
	2.3 Deflection Measurement	28
	2.4 Comparison of Predicted and Measured Refractive Effects	35
III.	VELOCITY MEASUREMENTS USING THE LDV	36
	3.1 Introduction	36
	3.2 Flammability Apparatus	37
	3.3 The Combustible Mixture	40
	3.4 Particle Seeding for the LDV	41
	3.5 The Laser Doppler Velocimeter	44
	3.6 Referencing System	50
	3.7 Experimental Procedure and Results	60
IV.	INTERRUPTED PARTICLE TRACKING (AN ALTERNATE METHOD)	67
	4.1 Introduction	67
	4.2 Experimental Arrangement	67
	4.3 Photographic Limitations and Optimization	69
V.	PREDICTING PERFORMANCE OF A 25 mW SYSTEM	72
VI.	RESULTS AND CONCLUSIONS	75
	References	77
	Appendix A	78
	Appendix B	79
	Appendix C	81

NOMENCLATURE

Note: Many intermediate angles and locations are defined as they are introduced in the text in the section where the deflection calculations procedure is described. They are not listed in this nomenclature list.

Letters

AN	Index of refraction of the transparent walls of an SFLT tube
$d_{e^{-2}}$	Diameter of LDV beam at location where its intensity is $1/e^2$ of the maximum intensity
d_f	Fringe spacing in the LDV viewing volume
d_p	Diameter of an LDV seed particle
D_a	Diameter of the light collecting aperture
f	Focal length of the LDV transmitting lens
Δf	Band width (frequency response) of photodetector
g	The constant of gravitational acceleration
G	Light scattering gain parameter
G_{BS}	Light scattering gain parameter for back scatter
G_{FS}	Light scattering gain parameter for forward scattering
L_i	Lean limit, in mole percent, of the ith component of a fuel mixture
L_m	Lean limit, in mole percent, of a fuel mixture
p_i	Mole percent of the ith component of a fuel mixture
P	Atmospheric pressure
P_m	Measured pressure at a rotometer
P_o	Power of the laser beam being used in an LDV system
r	Radius location of an undeflected LDV measuring volume in an SFLT
r_a	Distance from measuring volume to light collector

R_1	Inner radius of the SFLT
R_2	Outer radius of the SFLT
t	Time
V_t	The velocity of the gas that an LDV seed particle is immersed in
V_p	The velocity of an LDV seed particle
V_s	The final settling velocity of an LDV particle in the earth's gravitational field
V	Doppler signal visibility, i.e. amplitude of peaks to amplitude of pedestal
$\overset{o}{V}$	Flow rate calculated from a rotometer setting
$\overset{\cdot}{V}$	Flow rate indicated by a rotometer setting
V_{wheel}	Rotational velocity of a calibration wheel
Δx	Displacement of the LDV measuring volume in the x direction due to passage through the SFLT (negative values mean motion toward the source)
y_o	Off axis location of the undeflected LDV measuring volume
y_o'	Off axis location of the deflected LDV measuring volume

Greek letters

β	Angle between the beams that produce the LDV measuring volume
β'	Calculated angle between the beams that produce the LDV measuring volume after deflection by the SFLT tube walls
η_q	Quantum efficiency of a photo detector
Θ	Net rotation of the LDV measuring volume due to the deflection of the intersecting beams by passage through the walls of the SFLT
λ	Wave length of the laser light used in an LDV
μ	Viscosity of the gas that an LDV seed particle is immersed in
ν_D	Doppler frequency for a test of the system
ρ_f	Density of the gas in an LDV experiment
ρ_p	Density of an LDV seed particle
τ	Characteristic particle relaxation time for an LDV seed particle to respond to a step change in the gas velocity

Subscripts

o	Initial state
.015	15 mW laser power
2.0	2W laser power

Abbreviations and Acronyms

BDFD	Beam Deflection Flame Detector
LDV	Laser Doppler Velocimeter or Laser Doppler Velocimetry
NASA	National Aeronautics and Space Administration
SFLT	Standard Flammability Limit Tube
SNR	Signal to Noise Ratio
STP	Standard Temperature and Pressure
TSI	Thermal Systems Incorporated

ABSTRACT

The results of the study reported here have bearing on the use of the Laser Doppler Velocimeter, (LDV), to measure the flow associated with the passage of a flame through a Standard Flammability Limit Tube (SFLT). There are four major results of this study. These are:

1. It has been shown that using standard ray tracing calculations one can predict the displacement of the LDV volume and the fringe rotation within the experimental error of measurement.

2. The flow velocity vector field associated with passage of an upward propagating flame in an SFLT has been determined.

3. It has been determined that the use of a light interruption technique to track particles is not feasible.

4. It has been shown that a 25 mW laser would be adequate for LDV measurements in the Shuttle or Space Lab.

I

INTRODUCTION AND SYNOPSIS OF LDV THEORY

1.1 Introduction

Gaseous fuel-air mixtures exhibit a range of composition over which a flame will propagate spontaneously for long distances from a strong ignition source[1, 2]. These limits are apparatus dependent and they are strongly influenced by the earth's gravity field. Approximately 50 years ago the United States Bureau of Mines developed a "standard" flammability apparatus which consists of a vertical 51 mm interior diameter tube of approximately 1.8 meters length. For limit determination mixtures of fuel and air are placed in the tube. One end of the tube is then opened and ignition is effected at the open end. If the flame propagates the entire length of the tube the mixture is said to be flammable. If the flame extinguishes somewhere in the tube the mixture is said to be nonflammable and if the flame does not leave the region of the ignition source one is observing an ignition limit, not a flammability limit, due to the fact that the ignition energy is not sufficient to ignite a flame. It has been observed that in this flammability tube the limit is different for upward vs. downward propagation of the flame. In particular for the methane-air system the lean limit for upward propagation is 5.25% CH_4 while the lean limit for downward propagation 5.86% CH_4[3]. Also the shape of the downward propagating flame and the mechanism of extinction are markedly different than those for the upward propagating flame.

Because of the large effect of gravity on the nature of flame propagation and on the actual flammability limit in a standard flammability tube NASA Lewis Research Center has identified this experiment as one which should be studied under zero g conditions using either the Shuttle or Space Lab.

Preliminary studies to validate and define the usefulness of Shuttle or Space Lab experiments have been continuing for the past 4-5 years. Prior to the work reported in this report investigators at the University of Illinois have used a single beam Laser Doppler Velocimeter system to measure the vertical component of the flow velocity vector associated with the passage of the flame along the center line of the tube and have used holographic techniques to determine the density field associated with the flame and have photographed the extinction of the flame using an image intensifier[3]. All these experiments were performed under one g conditions. Additionally the behavior of the flame under zero g conditions was studied at NASA Lewis Research Center using the two second drop tower[3]. In these experiments the shape of the flame was photographed and its propagation speed through the tube was measured. Lean limits could not be determined however because under zero g conditions near the lean limit the flame had a propagation speed of only 5 cm/sec and thus traveled approximately 10 cm during the 2 second drop time. This distance of propagation was insufficient to say with certainty that extinguishment was really a flammability extinguishment and not an ignition extinguishment.

The purpose of the work that is reported herein is to 1) determine the effect of the presence of the plexiglass tube on the location of the Laser Doppler Velocimeter intersection volume and on the orientation of the fringes in that intersection volume, 2) simultaneously measure both the radial and the vertical components of the velocity vector during flame passage, 3) investigate the feasibility of using an interupted particle track technique to follow the flow associated with flame passage and 4) assess the feasibility of using a 25 mW Laser Doppler Velocimeter in the Shuttle or Space Lab to measure the flow velocity field associated with the passage of a flame under zero g conditions.

1.2 The Laser Doppler Velocimeter

A Laser Doppler Velocimeter is a tool which allows one to make nonintrusive measurements of the velocity of particles suspended in a fluid such as water or air. If these particles are small enough (diameter < 1 micrometer) they will follow the motion of the flow quite faithfully even under conditions where relatively high frequency turbulent fluctuations are occurring. The principle of the Laser Doppler Velocimeter is based on the fact that an optical laser produces a single frequency beam of coherent light of very high intensity and very small diameter. The word coherent here means that the light is oscillating in phase with itself just as the 60 cycle line current or the microwave signals that are used to transmit information. The principle of operation of the Laser Doppler Velocimeter is quite simple. A single beam of coherent light is split into two beams and these beams are aligned to be parallel to each other and some distance apart. Then these two beams are intercepted by a single lens whose center line lies exactly on the centerline of the two beams. This lens focuses the two beams at the same point in space producing an intersection volume in which the coherent nature of the light causes interference fringes to appear as shown in Fig. 1.

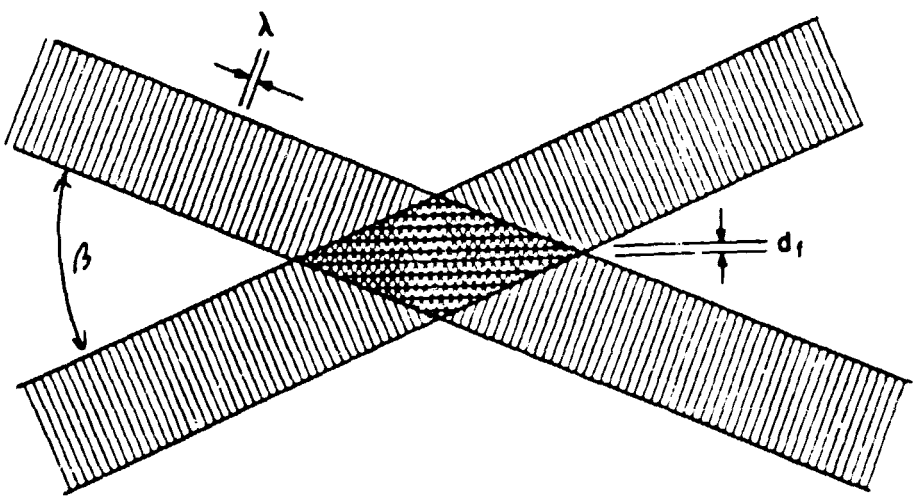

Figure 1. Representation of fringe pattern created by the intersection of two coherent light beams.

These stationary fringes are equally spaced and form planes that are perpendicular to the plane of the two incident beams. Spacing between the fringes is controlled by the wavelength of the light and their intersection angle,

$$d_f = \lambda \sin(\beta/2)$$

where d_f is the spacing, λ is the wavelength of the light, and β is the angle between the two incident beams. Since the beams themselves have essentially a Gaussian intensity distribution, the fringe region is actually a small double conical region in which the fringes have a Gaussian intensity distribution.

When a flow that is seeded with small particles passes through the beam each individual particle is illuminated by the interference pattern. A sensitive photomultiplier focused on the beam intersection volume will record the Doppler burst shown in Fig. 2. After the pedestal is removed the burst appears as shown in Figure 3. Here the overall amplitude envelope is essentially Gaussian in time and the frequency , f, of the internal signal yields the velocity component of the flow in the direction normal to the fringe orientation

$$u_x = d_f \cdot f$$

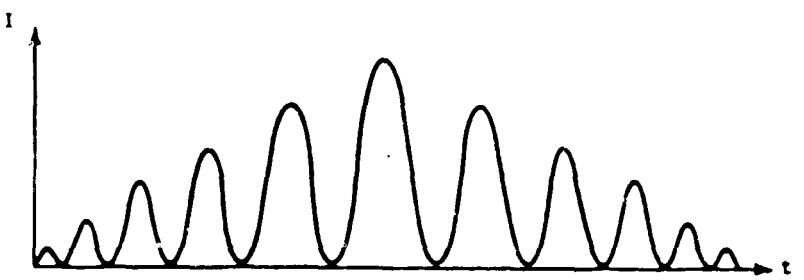

Figure 2. Doppler burst before pedestal removal.

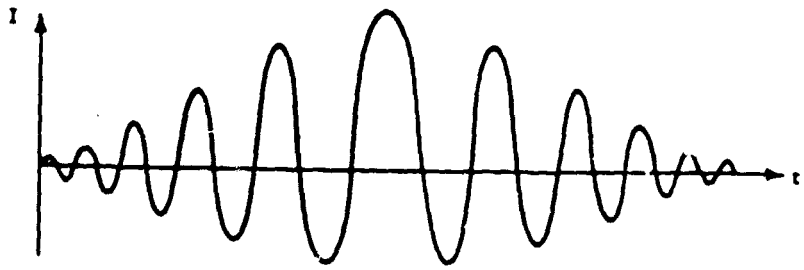

Figure 3. Doppler burst after pedestal removal.

It is obvious that with this type of arrangement one cannot discriminate between forward or reverse flow. This problem is handled by frequency shifting one of the beams using an optical technique. The frequency of that beam is usually shifted about 0.01 to 40 megahertz. This causes the fringes in the Doppler volume to travel through the volume at an extremely high velocity, much higher than any gas velocity that one would wish to observe. Thus, with frequency shifting, the frequency of the Doppler signal is increased markedly. Electronic instrumentation is used to subtract this frequency off the burst before it is analyzed. Using this technique one can discriminate between forward and backward flows as they pass through the Doppler volume.

In another innovation two laser beams of different colors are split into two pairs of parallel beams whose planes are orthogonal to each other and the lens now forms two sets of orthogonal fringes in the Doppler volume. Optical processing of the signal allows one to observe each of the two colored fringe patterns with two different photomultipliers and thus one can simultaneously obtain two components of the flow velocity at the same point in space.

The work presented in this report was performed using a two component frequency shifted Laser Doppler Velocimeter powered by a 2 watt Argon ion laser.

II

REFRACTIVE EFFECTS

2.1 Introduction

It is anticipated that either a one color or a two color laser Doppler system will be used to measure the flow velocities associated with flame passage in a standard flammability tube under zero g conditions. It is planned to orient the laser relative to the tube such that the beams will lie in vertical and horizontal planes (along the tube and across the tube) and the probe volumes will traverse the major axis of the tube that is orthogonal to the axis of the two beams. Thus, both the axial and radial components of the flow velocity will be measured along that axis. This will require a separate experiment for each location of the probe volumes. Unfortunately because the tube is circular and has a finite thickness and index of refraction the laser beams entering the tube will be deflected and will intersect at a location slightly removed from their intended intersection location. Also because the two beams enter the tube at different angles relative to the surface of the tube when the intersection volume is not at the center line of the tube the viewing volume may be slightly rotated because of passage through the plexiglass tube. For a vertical tube and the vertical set of intersecting beams the rotation of the viewing volume will not cause a rotation of the fringes because the fringes are in a horizontal plane. However, for the horizontal beam, the fringes are vertical and therefore rotation of the viewing volume will also cause a rotation of the orientation of the fringes. This means that the direction of the horizontal velocity vector that is measured will not be strictly radial.

2.2 Deflection Calculations

Ray tracing techniques can be used to calculate the effect of the plexiglass tube on all of these properties of the intersection volume. The calculation is reasonably complex and will be outlined step by step. First consider the case of horizontal beams in a vertical tube. Figure 4 shows the upper beam (in the drawing) at an angle alpha to the center line of the tube, intersecting the outer tube wall, of radius R_2, at a point A and placed so as to intercept the major axis of the circular tube at point B if no deflection were to occur.

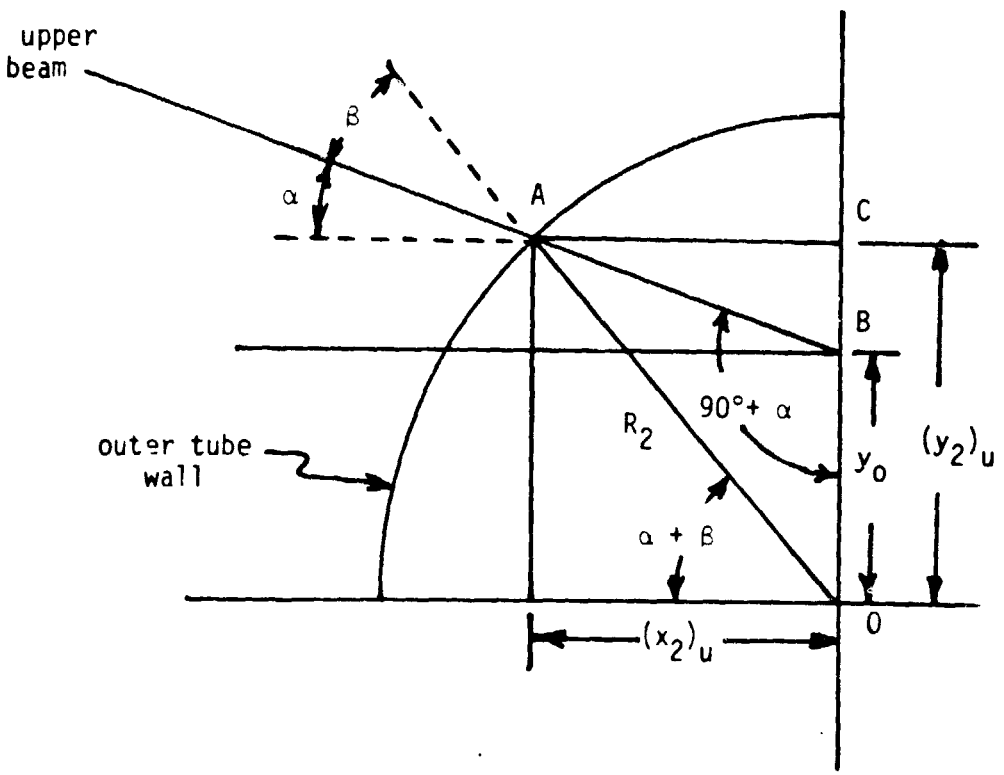

Figure 4. Location of the upperbeam intersection with outer tube wall when undeflected beam is displaced a distance y_o (point B from the center of the tube, 0).

This point B is a distance y_o above the center of the tube, 0. The angle beta, which is the angle between the ray and a normal to the surface of the tube where it enters the tube, can be determined by using the sine law:

$$\frac{y_o}{\sin \beta} = \frac{R_2}{\sin (\alpha + 90^0)}$$

or

$$\beta = \arcsin \left[\frac{y_o}{R_2} \sin (\alpha + 90^0)\right]$$

Then the triangle ACO in Figure 4 can be used to calculate the location of the point at which the beam intercepts the outside wall of the tube.

$$(y_2)_u = R_2 \sin (\alpha + \beta)$$
$$(x_2)_u = R_2 \cos (\alpha + \beta)$$

Since the index of refraction of the tube material is higher than that of air the entering beam will be deflected in a direction towards the local normal to the surface of the tube. In other words the angle delta in Figure 5 will be less than the angle beta.

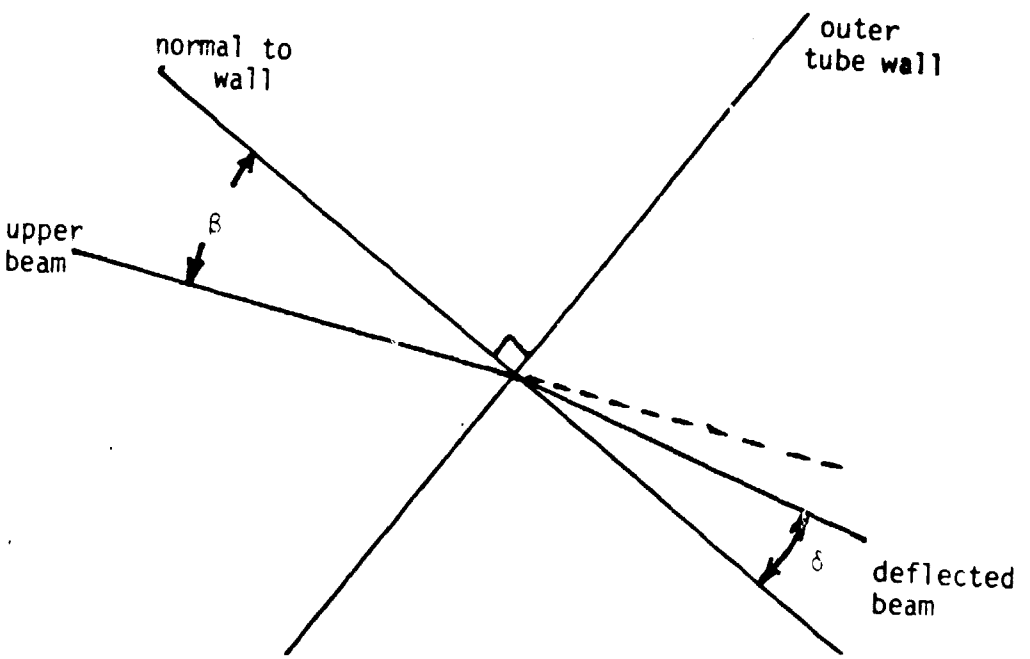

Figure 5. A schematic drawing of the index of refraction law AN = sin β/sin δ.

The index of refraction law yields the relationship

$$\delta = \arcsin\left[\frac{1}{AN}\sin\beta\right]$$

where AN is the index of refraction. We must now find the location of the beam when it intercepts the inner surface of the tube and the angle that it makes relative to the normal to the inner surface of tube at the point where it exits the tube wall. Figure 6 shows the construction for that calculation.

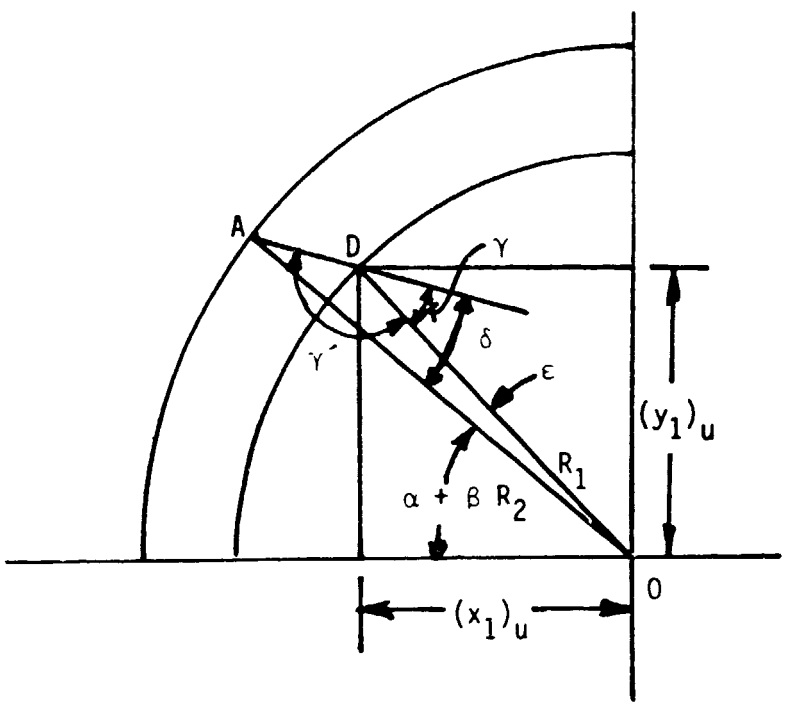

Figure 6. The location of the intersection of the light beam with the inner surface of the tube (point D).

The sine law can be used to determine γ' which is somewhat less than 180°. If we use the principle value of gamma, γ = 180 - γ', since sin γ = sin (180 - γ') we obtain the relationship

$$\gamma = \arcsin\left[\frac{R_2}{R_1}\sin\delta\right]$$

and we can calculate the angle epsilon using the relationship

$$\varepsilon = \gamma - \delta$$

We note from Figure 6 that we can now determine the (x, y) location of the point at which the beam exits the tube as well as the exit angle relative to the y = 0 axis.

$$(y_1)_u = R_1 \sin(\alpha + \beta + \varepsilon)$$

$$(x_1)_u = R_1 \cos(\alpha + \beta + \varepsilon)$$

We must now calculate the angle to the x axis that the beam makes when it exits the tube wall. Referring to Figure 7 the index of refraction law states that

$$\eta = \arcsin[AN \sin \gamma]$$

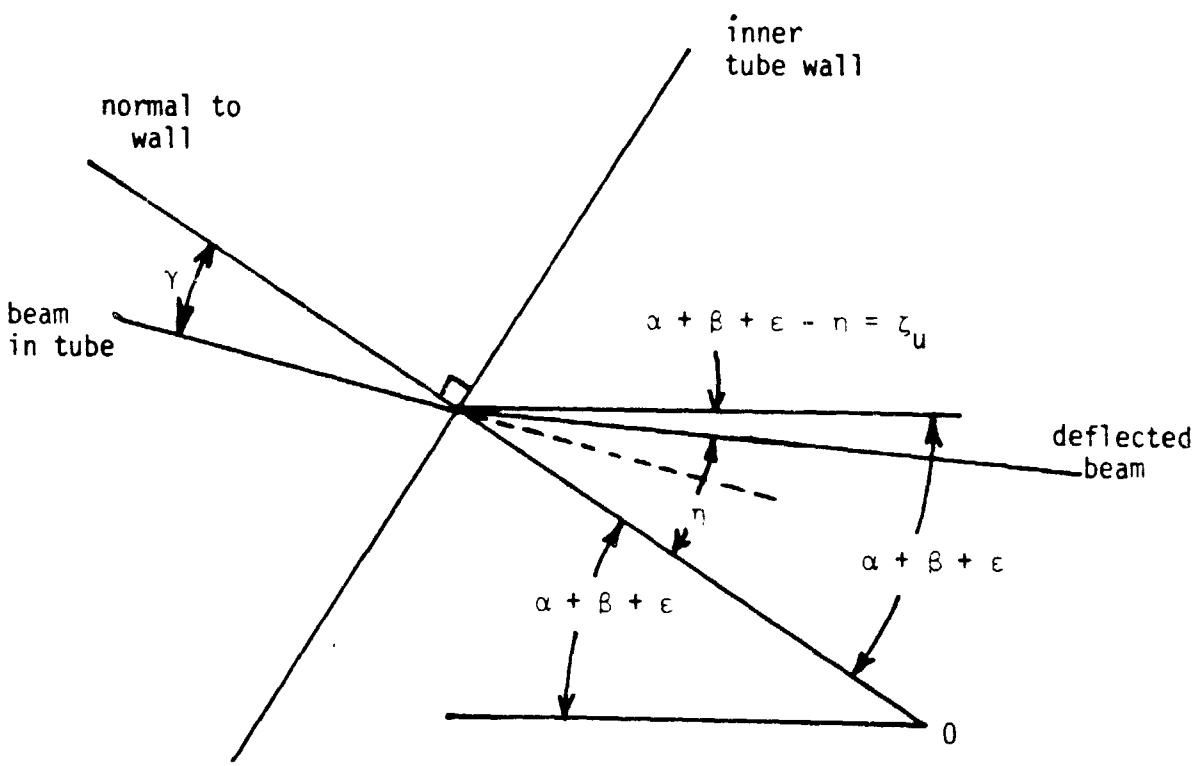

Figure 7. The angle at which the upper beam emerges from the inner wall (ζ_u)

and the geometry of Figure 7 shows that the desired angle ζ_u is given by the relationship

$$\zeta_u = \alpha + \beta + \varepsilon - \eta$$

For the lower beam the geometry is only slightly different. Notice from Figure 8 that for the lower beam the angle that was 90 + α for the upper beam becomes 90 - α.

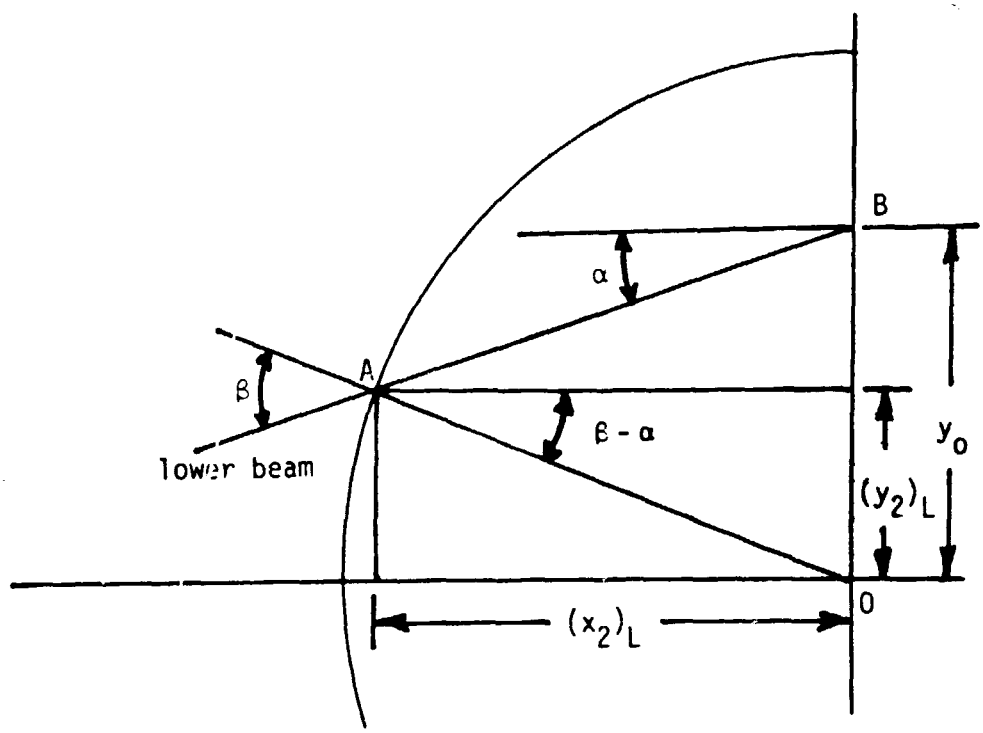

Figure 8. The calculation of the location of the point that the beam intercepts the wall (point A) for the lower beam.

However, sin (90 + α) = sin (90 - α). Thus β and δ are equal for the upper and lower beam for the same displacement y_o. This means the γ and ε are also equal for the upper and lower beam. However the location of the intersection of the lower beam with the outer wall of the tube must be calculated using the equations

$$(y_2)_L = R_2 \sin(\beta - \alpha)$$
$$(x_2)_L = R_2 \cos(\beta - \alpha)$$

its exiting location must be calculated using the equations

$$(y_1)_L = R_1 \sin(\beta - \alpha + \varepsilon)$$
$$(x_1)_L = R_1 \cos(\beta - \alpha + \varepsilon)$$

and its exit angle using the equation.

$$\zeta_L = \beta - \alpha + \varepsilon - \eta$$

Figure 9 shows how the intersection point, the intersection half angle, and the rotation of the viewing volume is calculated.

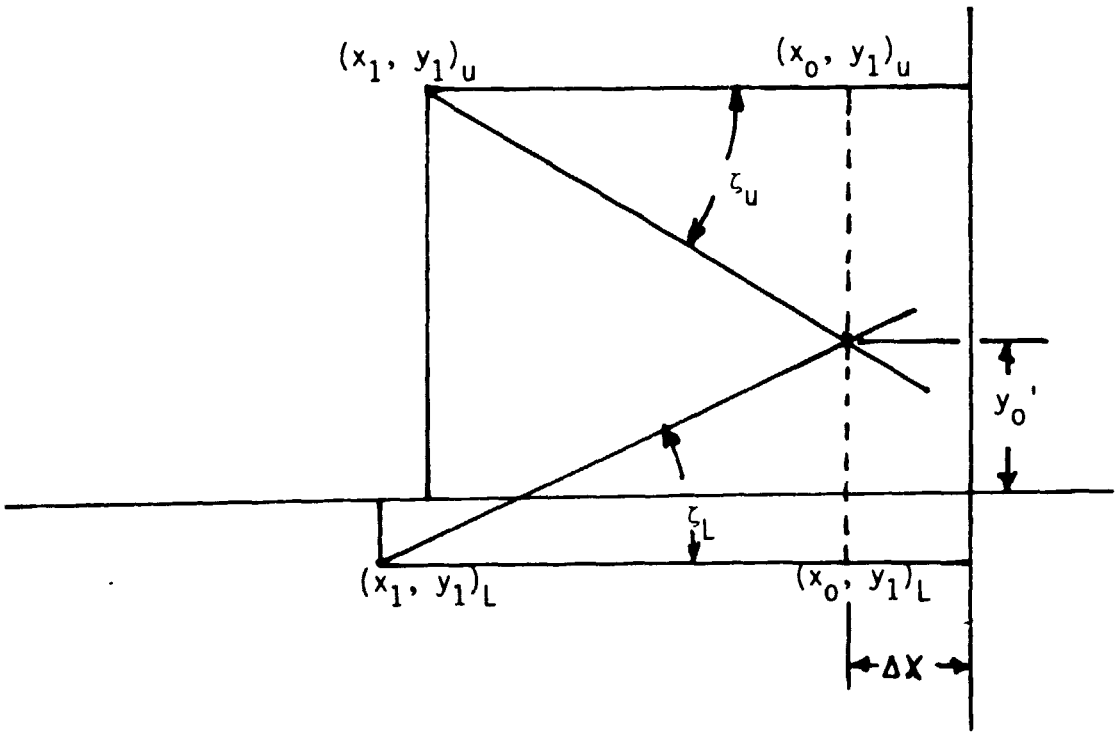

Figure 9. The geometry used to calculate the actual location of the intersection volume.

Since ζ_L is negative we can define two ratios

$$A = \tan(\zeta_u) = \frac{(y_1)_u - y'_o}{(x_1)_u - x_o}$$

and

$$B = \tan(-\zeta_L) = \frac{y'_o - (y_1)_L}{(x_1)_L - x_o}$$

We therefore have two equations in two unknowns

$$A(x_1)_u - Ax_o = (y_1)_u - y'_o$$

and

$$B(x_1)_L - Bx_o = y'_o - (y_1)_L$$

which can be solved for x_o and y_o' to yield

$$x_o = \frac{(y_1)_L - (y_1)_u + A(x_1)_u + B(x_1)_L}{(A + B)}$$

and

$$y_o' = (y_1)_L + B[(x_1)_L - x_o]$$

Therefore the displacement of the beams intersection point is given by

$$\Delta x = -x_o$$

and

$$\Delta y = y_o' - y_o$$

The half angle between the two beams is given by

$$\beta'/2 = (\zeta_u - \zeta_L)/2$$

and the net rotation by the equation

$$\theta = (\zeta_u + \zeta_L)/2$$

A computer program was written to perform these calculations. It is listed in Appendix A. A tabulation of these calculated values is given in Table I for a beam half angle of 10.8° and in Table II for a half angle of 5.515°. Their import will be discussed after the calculation for the vertical beams and the experimental measurement of deflections are presented.

TABLE I

Effect of plexiglass tube on location and rotation
of the horizontal beam intersection volume
(for half angle of 10.8°)
(refer to Figure 9)

y_o, mm	y'_o, mm	Δx, mm	θ, deg	$\beta'/2$, deg
0.0	0.000	0.000	0.000	10.80
1.0	1.000	-.001	-.082	10.80
2.0	2.000	-.006	-.165	10.80
3.0	3.000	-.013	-.250	10.80
4.0	4.000	-.024	-.337	10.80
5.0	5.000	-.038	-.426	10.80
6.0	6.000	-.055	-.520	10.80
7.0	7.000	-.077	-.619	10.80
8.0	7.999	-.102	-.724	10.80
9.0	8.999	-.133	-.837	10.80
10.0	9.999	-.170	-.959	10.80
11.0	10.998	-.213	-1.093	10.80
12.0	11.997	-.263	-1.240	10.80
13.0	12.996	-.323	-1.405	10.80
14.0	13.995	-.394	-1.590	10.80
15.0	14.993	-.478	-1.801	10.80
16.0	15.990	-.579	-2.045	10.80
17.0	16.987	-.701	-2.331	10.80
18.0	17.982	-.851	-2.672	10.80
19.0	18.975	-1.037	-3.088	10.80
20.0	19.964	-1.275	-3.606	10.80
21.0	20.948	-1.586	-4.273	10.80
22.0	21.921	-2.009	-5.170	10.79
23.0	22.876	-2.622	-6.457	10.79
24.0	23.786	-3.604	-8.520	10.79
25.0	24.564	-5.631	-12.840	10.79

TABLE II

Effect of plexiglass tube on location and rotation
of the horizontal beam intersection volume
(for half angle of 5.515°)
(refer to Figure 9)

y_o, mm	y'_o, mm	Δx, mm	θ, deg	$\beta'/2$, deg
0.0	0.000	0.000	0.000	5.515
1.0	1.000	-.001	-.083	5.515
2.0	2.000	-.006	-.168	5.515
3.0	3.000	-.013	-.253	5.515
4.0	4.000	-.024	-.341	5.515
5.0	5.000	-.038	-.433	5.515
6.0	6.000	-.056	-.528	5.515
7.0	7.000	-.078	-.629	5.515
8.0	7.999	-.104	-.736	5.515
9.0	8.999	-.136	-.851	5.515
10.0	9.999	-.173	-.977	5.515
11.0	10.998	-.217	-1.114	5.515
12.0	11.997	-.269	-1.265	5.515
13.0	12.996	-.330	-1.435	5.515
14.0	13.995	-.403	-1.627	5.515
15.0	14.993	-.490	-1.847	5.515
16.0	15.990	-.595	-2.102	5.515
17.0	16.986	-.722	-2.403	5.515
18.0	17.981	-.880	-2.764	5.515
19.0	18.973	-1.077	-3.208	5.515
20.0	19.961	-1.331	-3.766	5.515
21.0	20.942	-1.668	-4.496	5.515
22.0	21.912	-2.136	-5.496	5.515
23.0	22.857	-2.831	-6.977	5.515
24.0	23.742	-4.014	-9.498	5.515
25.0	24.404	-7.143	-16.374	5.515

Determining the effect of off-axis behavior on the deflection of the vertical beams is a considerably more complex problem than determining the deflection of the horizontal beams. In this case since both beams enter the tube at the same off-axis location and the same angle to the horizontal they will both be deflected in an identical manner (as mirror images). As with the horizontal beams the elevation of the intersection volume (i.e. the z direction) will not be displaced. Figure 10 is a three dimensional drawing illustrating the geometry used to calculate the refraction of the beam when it enters the tube wall. The angle alpha in this figure lies in a horizontal plane and the angle 10.8° is the half angle of the two beams and lies in the vertical plane. The angle beta lies in a plane which contains the beam and the normal to the wall surface at point 0. This plane is tilted by an angle gamma to the horizontal plane. This plane also contains the refracted beam inside the wall and the refracted beam inside the tube itself. The first step in the calculation is to determine the location of the point at which the beam intersects the tube wall relative to the center of the tube at z = 0. Referring to Figure 11, for a horizontal displacement of the beam y_o the angle alpha and the location (x_2, y_2, z_2) can be calculated using the equations

$$\alpha = \arcsin (y_o/R_2)$$

$$x_2 = R_2 \cos\alpha$$

$$y_2 = y_o$$

$$z_2 = x_2 \tan 10.8$$

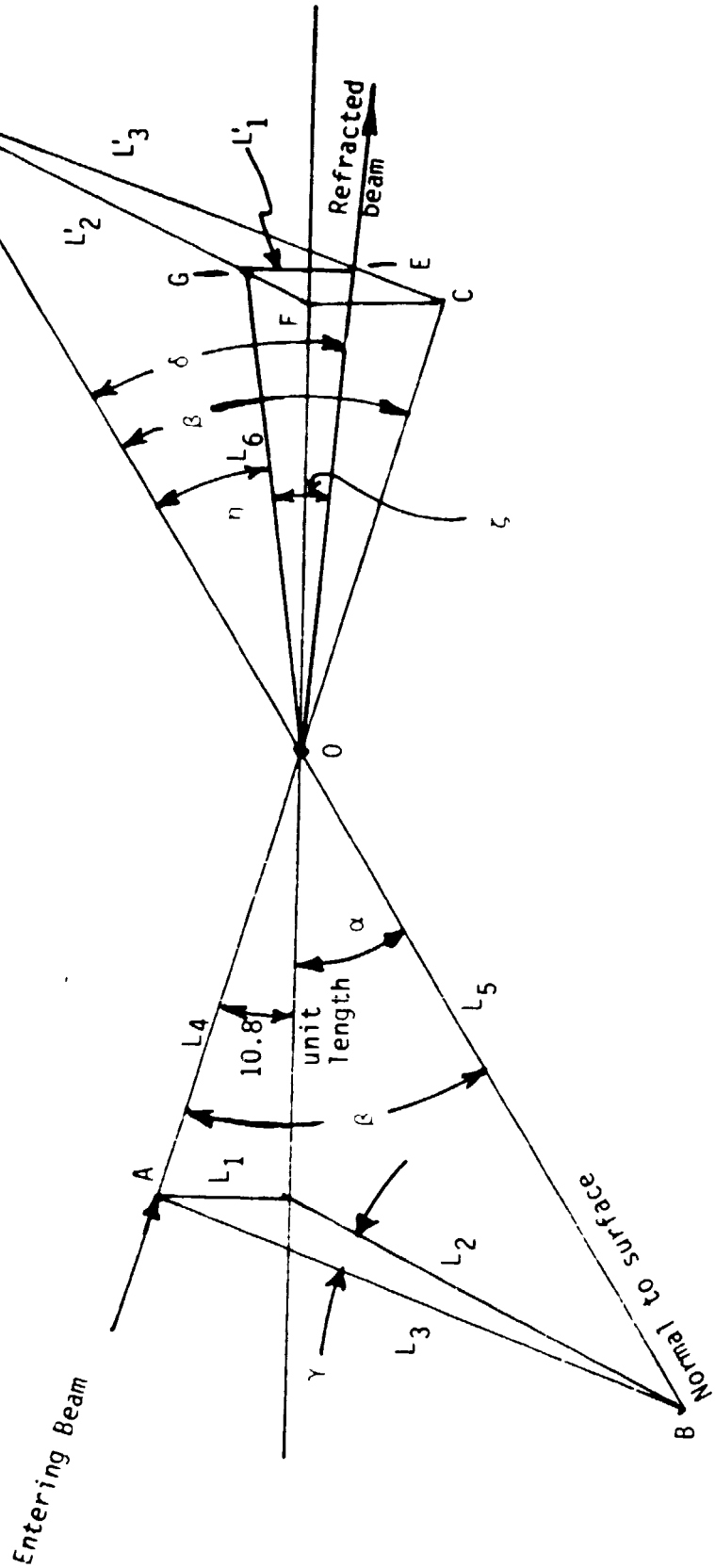

Figure 10 The geometry when a beam in the vertical plane enters the tube at an off axis position

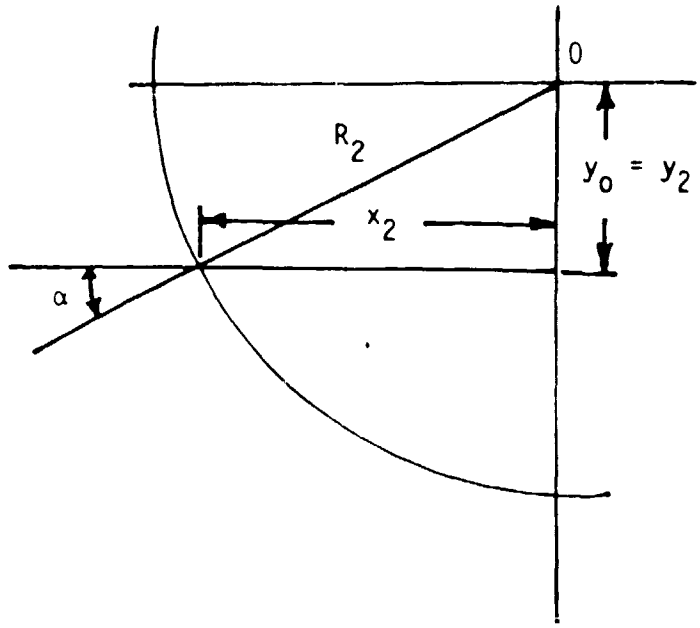

Figure 11. Location of the intersection point of the beam in the vertical plane with the outside surface of the tube and the angle, α, that the beam makes with that surface in the horizontal plane

Now referring back to Figure 10, if we assume that the line segment AO has unit length we can calculate the angles beta and gamma using the following formulas

$$L_1 = \tan 10.8$$

$$L_2 = \tan \alpha$$

$$L_3 = \sqrt{L^2_1 + L^2_2}$$

$$L_4 = \sqrt{1 + L^2_1}$$

$$L_5 = \sqrt{1 + L^2_2}$$

$$\gamma = \arctan (L_1/L_2)$$

$$\beta = \arccos \frac{L^2_4 + L^2_5 - L^2_3}{2L_4L_5}$$

The index and refraction law and the angle beta may now be used to calculate the angle delta which lies in the plane OCED inside the tube wall.

$$\delta = \arcsin \left[\frac{1}{AN} \sin \beta\right]$$

As stated earlier, this plane is the same plane as the plane AOB that contains beta. However, on this side of the point O this plane is below the horizontal plane OFGD. In order to continue the calculation the angle delta must be re-resolved back into the angles eta and zeta which lie in the horizontal and vertical planes, respectively. Figure 12 is a drawing of the OCED plane and it illustrates how the value of the angle epsilon and the length L_3' are calculated using the following equations

$$\omega = \arcsin \left[\frac{L_4}{L_3} \sin\beta\right]$$

$$\varepsilon = (180 - \delta - \omega)$$

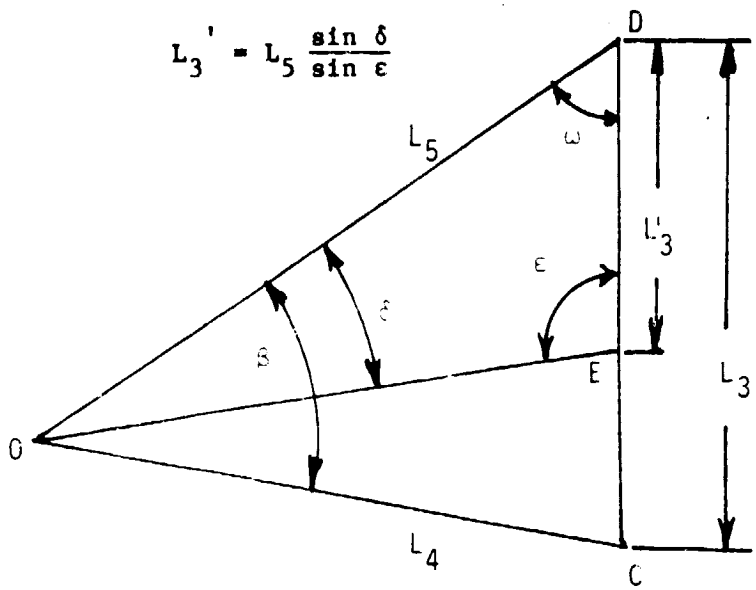

Figure 12. Geometry for the calculation of ε and the length L_3' in the COD plane. Note that in general there are no right angles in these triangles.

Specifically, the angle omega is calculated using the sin law. Epsilon is determined for the triangle OED and L_3' is calculated using the sin law in the triangle OED. Next notice that the triangle DFC and the included triangle DGE shown on Figures 10 and 13 are similar triangles. This allows the calculation of L_2'.

$$L_2' = L_2 L_3'/L_3$$

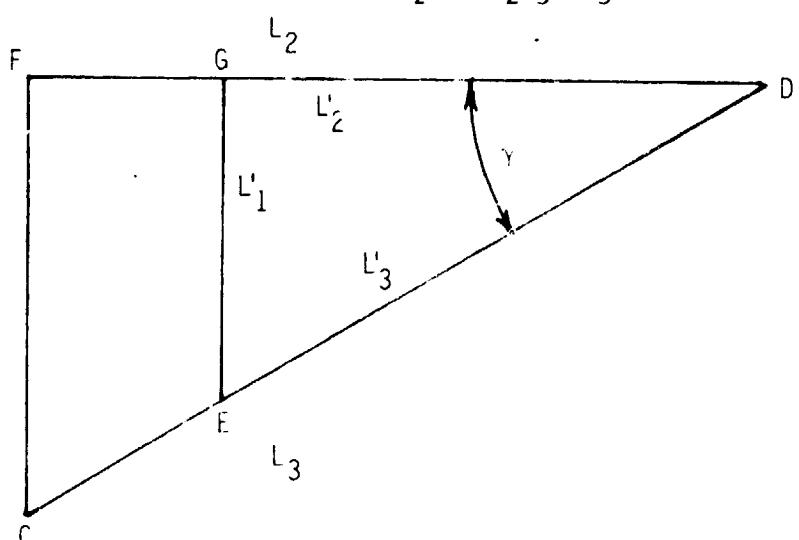

Figure 13. The geometry used to calculate L_2'.

In Figure 14 the triangle OFGD is drawn and used to calculate the value of eta.

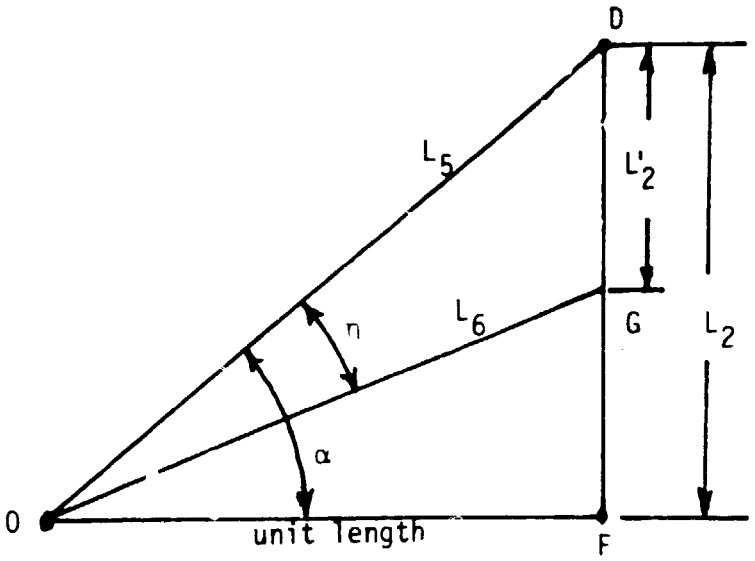

Figure 14. Geometry for the calculation of η in the OFGD plane. Note that the angle OFD is a right angle in this plane.

$$(\alpha - \eta) = \arctan (L_2 - L_2')$$

or

$$\eta = \alpha - \arctan (L_2 - L_2')$$

Note that eta is the angle the refracted beam makes to the vertical plane that runs through the normal to the surface. The length of the lines OG and GE are then calculated to allow the determination of the angle zeta

$$L_6 = 1.0/\cos (\alpha - \eta)$$

Referring back to Figures 10 and 13 the length L_1' can now be calculated and this allows the determination of zeta, which is the angle the refracted beam makes to the horizontal plane.

$$L_1' = L_2' \tan \gamma$$

$$\zeta = \arctan (L_1'/L_6)$$

We next need to determine the location where the beam exits the wall to enter the tube. Figure 15 shows the geometry associated with this problem.

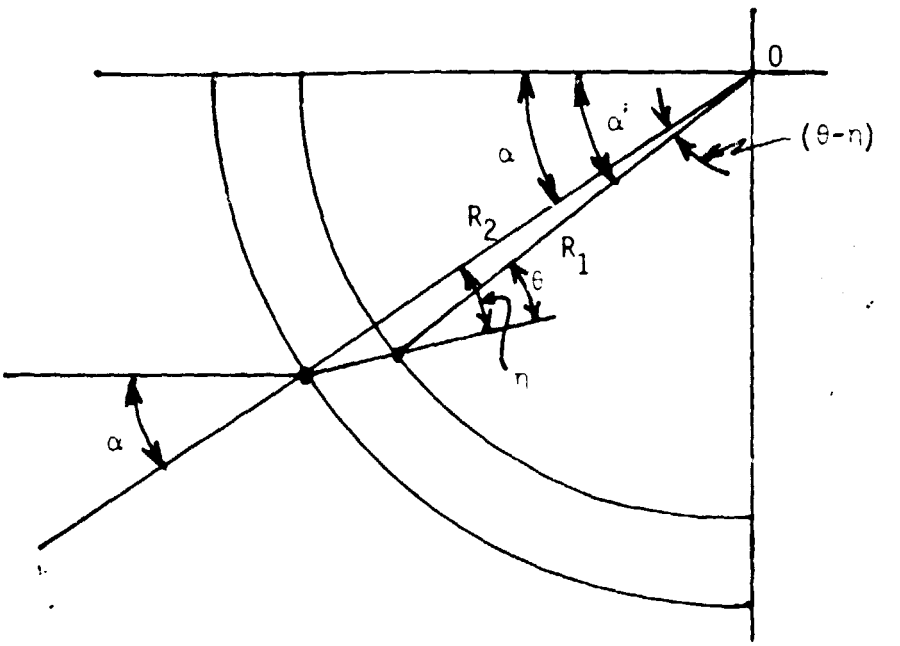

Figure 15. Calculations of the angular and (x_1, y_1) position when the beam exits the wall.

The sin law can be used to calculate the value of the angle theta and simple addition can be used to determine the angle alpha' at which the beam exits the wall.

$$\frac{R_1}{\sin \eta} = \frac{R_2}{\sin (180 - \theta)} = \frac{R_2}{\sin \theta}$$

therefore

$$\theta = \arcsin [(R_2/R_1) \sin \eta]$$

and

$$\alpha' = \alpha + \theta - \eta$$

Figure 15 also illustrates the geometry used to calculate the locations (x_1 and y_1) where the beam exits the wall.

$$x_1 = R_1 \cos \alpha'$$

$$y_1 = R_1 \sin \alpha'$$

The value of z_1 can be determined by calculating the path length of the beam in the plexiglass tube wall and noting that its angle to the horizontal plane passing through a normal to the surface in the tube is given by the angle zeta.

$$P = \sqrt{[(x_2 - x_1)^2 + (y_2 - y_1)^2]}$$

$$z_1 = z_2 - P \tan \zeta$$

To determine the exit angle for the beam in the horizontal and vertical planes we can use the same procedure as was used to determine the angles eta and zeta, only now the entrance angle, 10.8, becomes the angle zeta and the off-axis angle normal to the surface, alpha, becomes the angle theta. The geometry is identical to the geometry used to calculate the behavior of the beam when it entered the tube wall, except that nes values of eta prime and zeta prime are calculated after using the index refraction formula for the exiting beam

$$\delta' = \arcsin (AN \sin\beta')$$

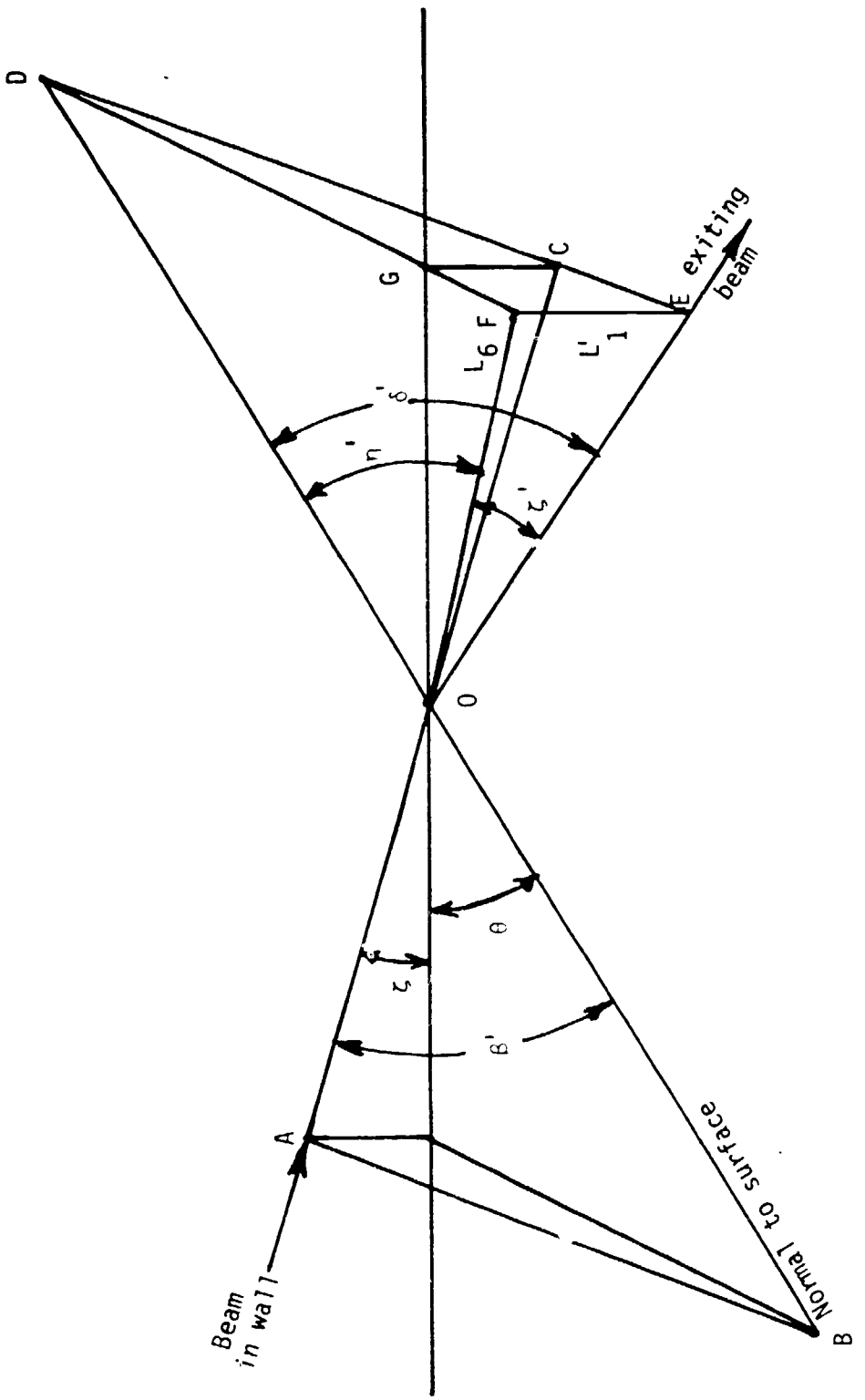

Figure 16 The geometry that defines the direction of the beam as it exits the tube wall and enters the tube. Note that the angle 10.8 in figure 9 becomes ξ and the angle α in figure 9 becomes 0. Also note that $\delta > \Theta$.

Figure 16 is a three dimensional drawing similar to Figure 10 except that it shows that when the beam exits the tube wall to enter the tube the refracted beam OE exits at an angle to the normal to the surface which is larger than the incident beam AO. This is because the index of refraction of the gas in the tube is less than that of the wall. Figure 17 shows the geometry that is used to calculate the x location of the beam intersection point.

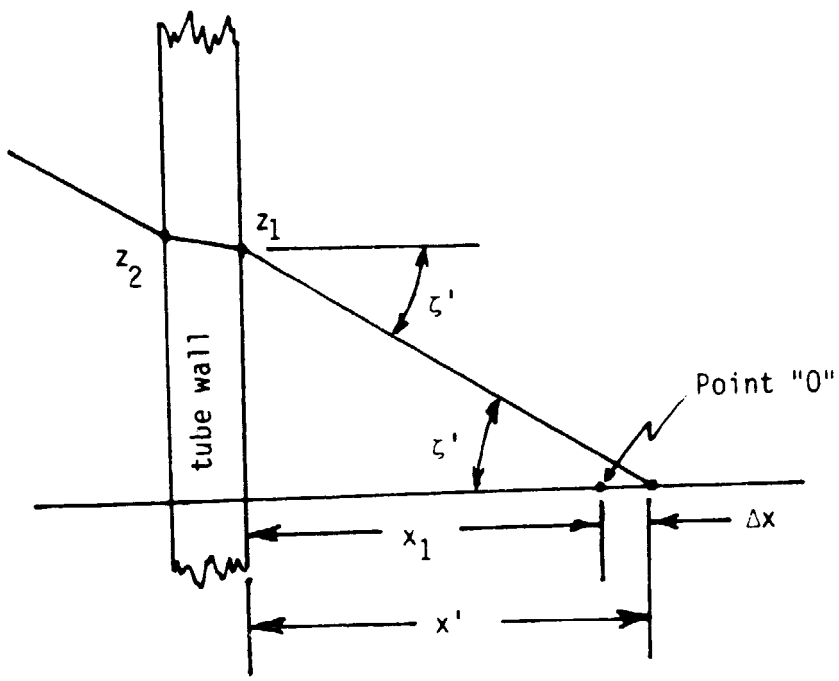

Figure 17. Geometry used to calcuate Δx for the vertical beam intersection volume.

The location of the intersection point x' and the Δx displacement of this location may be calculated using the following formula.

$$\Delta x = x_1 - x' = x_1 - z_1/\tan \zeta'$$

The geometry for calculating the lateral displacement and rotation of the beam is shown in Figure 18. The equations for this calculation are as follows. For the beam rotation

$$\Theta = \alpha' - \eta'$$

and for the lateral displacement

$$y_o' = y_1 + x_1' \tan \Theta$$

A separate computer program was written to perform the calculations for the vertical beams. It is listed in Appendix B. Tables III and IV contain the results of these calculations for the vertical beams. Their import will be discussed in section 2.4 after the presentation of the measured deflections.

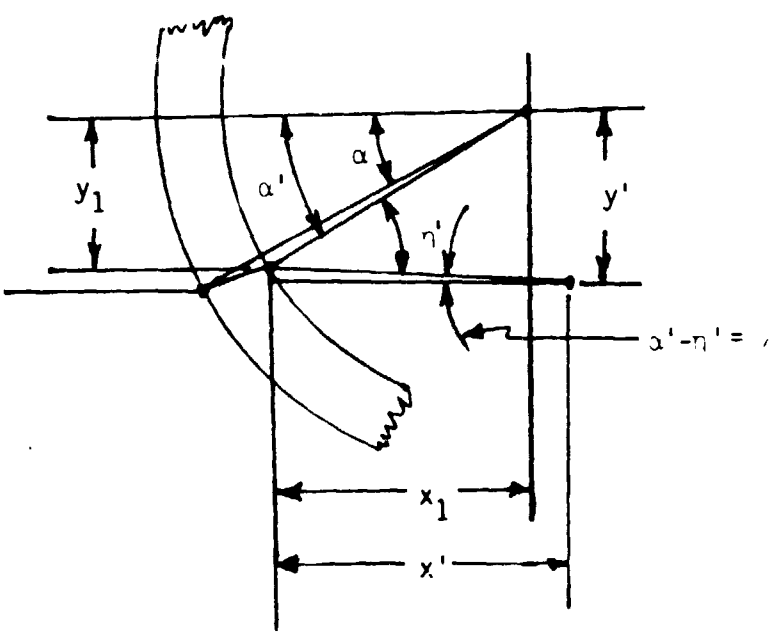

Figure 18. The geometry used to calculate the angle of rotation of the beam ($\alpha' - \delta'$) and the actual (y') location of the intersection volume.

TABLE III

Effect of plexiglass tube on the location and rotation of the vertical beam intersection volume (for a half angle of 10.8°) (refer to Figure 18)

y_o, mm	y'_o, mm	Δx, mm	θ, deg	$\beta'/2$, deg
0.0	0.000	-1.065	0.000	10.80
1.0	1.018	-1.065	-.096	10.80
2.0	2.036	-1.066	-.194	10.80
3.0	3.053	-1.068	-.292	10.80
4.0	4.071	-1.070	-.394	10.80
5.0	5.090	-1.073	-.499	10.80
6.0	6.108	-1.076	-.609	10.80
7.0	7.126	-1.080	-.726	10.80
8.0	8.145	-1.085	-.849	10.80
9.0	9.164	-1.090	-.982	10.80
10.0	10.184	-1.096	-1.126	10.80
11.0	11.204	-1.102	-1.284	10.80
12.0	12.224	-1.109	-1.458	10.80
13.0	13.246	-1.116	-1.652	10.80
14.0	14.268	-1.124	-1.872	10.80
15.0	15.292	-1.131	-2.124	10.80
16.0	16.319	-1.139	-2.416	10.80
17.0	17.347	-1.147	-2.759	10.80
18.0	18.380	-1.154	-3.172	10.80
19.0	19.418	-1.161	-3.677	10.80
20.0	20.466	-1.167	-4.312	10.80
21.0	21.527	-1.170	-5.142	10.80
22.0	22.616	-1.170	-6.281	10.80
23.0	23.759	-1.165	-7.973	10.80
24.0	25.054	-1.152	-10.899	10.80
25.0	28.017	-1.126	-22.760	10.80

TABLE IV

Effect of plexiglass tube on the location and rotation of the vertical beam intersection volume (for a half angle of 5.515°) (refer to Figure 18)

y_o, mm	y'_o, mm	Δx, mm	θ, deg	$\beta'/2$, deg
0.0	0.000	-1.050	0.000	5.515
1.0	1.018	-1.050	-.095	5.515
2.0	2.036	-1.051	-.191	5.515
3.0	3.053	-1.052	-.288	5.515
4.0	4.071	-1.055	-.388	5.515
5.0	5.089	-1.057	-.492	5.515
6.0	6.107	-1.061	-.601	5.515
7.0	7.126	-1.065	-.715	5.515
8.0	8.145	-1.070	-.837	5.515
9.0	9.163	-1.075	-.968	5.515
10.0	10.183	-1.081	-1.110	5.515
11.0	11.203	-1.087	-1.266	5.515
12.0	12.223	-1.094	-1.438	5.515
13.0	13.245	-1.102	-1.631	5.515
14.0	14.267	-1.109	-1.849	5.515
15.0	15.291	-1.117	-2.098	5.515
16.0	16.317	-1.126	-2.387	5.515
17.0	17.346	-1.134	-2.727	5.515
18.0	18.378	-1.142	-3.136	5.515
19.0	19.416	-1.149	-3.637	5.515
20.0	20.463	-1.155	-4.269	5.515
21.0	21.524	-1.159	-5.094	5.515
22.0	22.611	-1.160	-6.228	5.515
23.0	23.753	-1.156	-7.914	5.515
24.0	25.045	-1.144	-10.832	5.515
25.0	27.998	-1.119	-22.685	5.515

2.3 Deflection Measurement

To check the calculations, experiments were performed to photograph the beams as they were refracted by the tube. A 40 cm section of tubing with properties identical to those of the Standard Flammability Limit Tube (SFLT) was used for the experiments. It was a transparent polymethylmethacrylate tube, having an inside diameter of 50.72 mm, a thickness of 2.79 mm, and a refractive index of 1.49.

Because the refractive effects were small in relation to the corresponding amount of off-axis positioning, accurate alignment of the tube section with the laser beams was necessary. Figure 19 depicts the arrangement for refraction measurements of the horizontal beams. A 79 cm x 137 cm table which translated in two dimensions was used to act as a moving support for the tube section and photographic system. The laser beam source and transmitting lens were fixed so that movement of the table in the Y-direction would move the tube for off-axis measurements.

Both the horizontal and vertical beams were used for alignment. The table surface was first carefully leveled to form a horizontal plane parallel to and about 3 cm below the plane formed by the two horizontal beams. The two axes of table translation were aligned along the X and Y axes as defined in Fig. 19. Alignment was accomplished without the SFLT in place by positioning a mirror mounted 90 degrees to the table surface at the beam crossing, facing the transmitting lens as shown in Figure 20. When the table was properly oriented, the reflected beams coincided with the incident beams and translation of the table along the Y axis did not alter beam coincidence. Translation of the table in the negative X direction (toward the lens) caused the four reflected beams to form a perfectly centered rectangular pattern inside the location of the incident beams on the lens surface.

A 90 degree draftsman triangle was used to check the table alignment with respect to the vertical beams, as shown in Fig. 21. When the table was properly aligned, the vertical edge of the triangle would just "touch" both beams simultaneously as the table was translated to the right.

Once the table was aligned, a flat front surface mirror was laid face up on it directly below the beam crossing. The 40 cm long SFLT section was mounted directly above the mirror. The tube was adjusted to be perfectly vertical by aligning it with its reflection in the horizontal mirror.

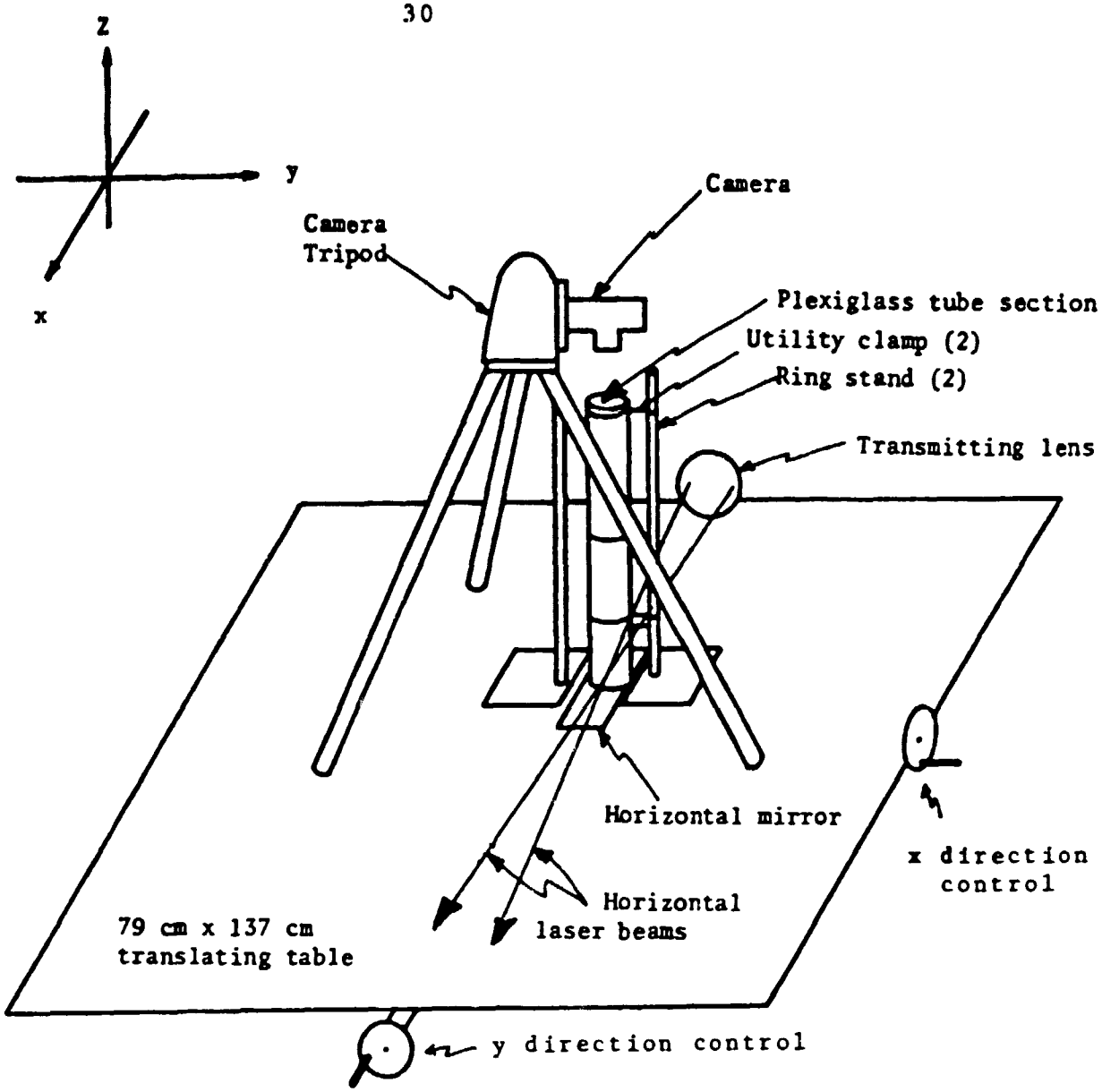

Figure 19 Arrangement for horizontal refraction measurements.

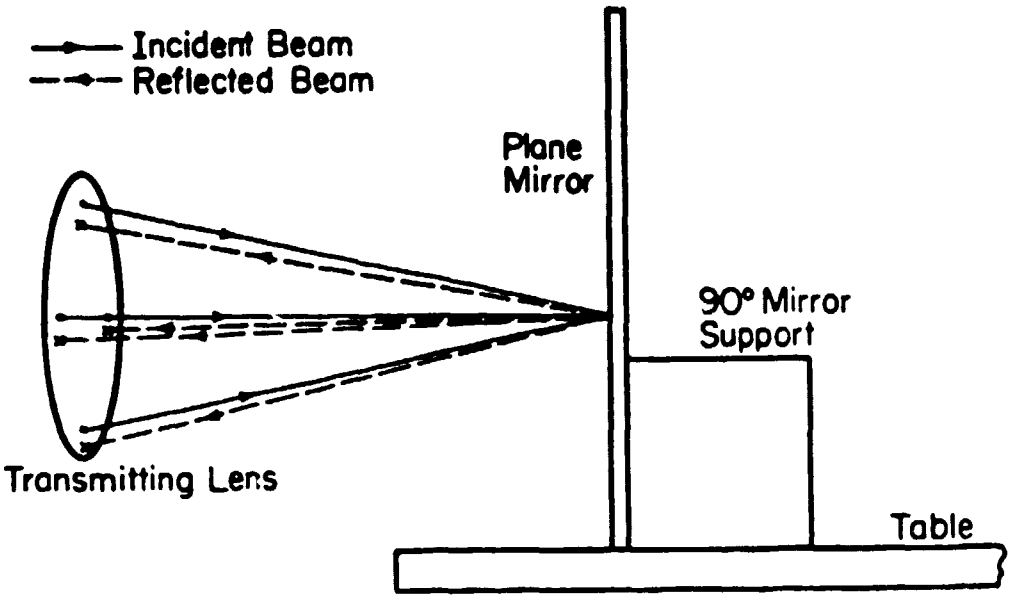

Figure 20 Alignment test of laser beams with table. Drawing depicts table tilted slightly forward.

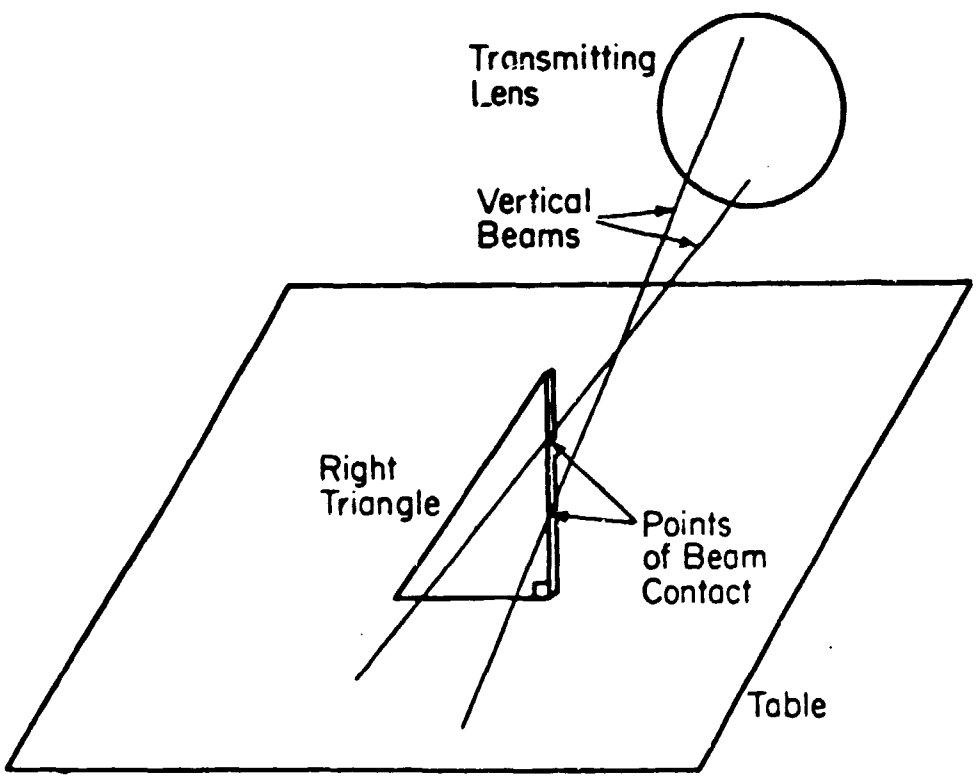

Figure 21 Arrangement for table alignment with vertical beams.

The vertical beams were blanked off and the horizontal beams were photographed with a Canon A-1 35 mm camera with a Vivitar 210 mm telephoto lens and #1 close-up lens attachment. The camera was mounted on a tripod approximately 10 cm above the tube top, as shown in Fig. 19. To position the camera to look directly down the tube axis, the reflection of the camera lens in the horizontal mirror was centered in the camera field of view. This oriented the film plane in the camera normal to the tube axis. The camera was then moved horizontally until the reflection of the lens lay exactly in the center of the image of the tube bottom. This procedure centered the camera directly over the tube axis.

The circular inside edge of the tube bottom served as a reference in making measurements from the photographs. Since the horizontal beams were only 1 cm above the tube bottom, the camera system operating at f8 provided adequate depth of field. The distance from the camera film plane to the beams was 50 cm, and to the tube bottom, 51 cm. Parallax effects in the measurements were accounted for.

To check flatness of field, a fine grid was photographed with the above photographic system from a distance of 50 cm, and the negative was measured on the Bausch & Lomb 10x optical comparator. The grid spacing was found to be constant in the 50 mm diameter region of concern.

The alignment procedure for the measurement of horizontal refraction has been described. The procedure for vertical refraction measurements was similar because the vertical position y'_o and deflection angle θ could be measured using the set up shown in Fig. 19. The only difference was that the camera had to be mounted horizontally to view the tube from the -Y side to determine values of Δx. To avoid obtaining a refracted image of the already refracted beams, a 60 degree arc centered on the -Y axis was cut out of the

tube and measurements were made of the beams on the +Y side of the tube.

To conduct the measurements, the beams must be centered in the tube with high precision. The transmitting optics were first translated in the y direction of Fig. 19 until all secondary beam reflections formed a symmetric pattern on the tube walls. This located the probe volume on the x axis to an accuracy of ± 0.06 mm in the y direction. The table was then translated in the positive and negative x directions until the refracted and reflected horizontal converging beams formed two single spots on the opposite inside walls. The table position was measured with metric dial gages, and the tube center was assumed to be located exactly at this point. Accuracy of centering the probe volume on the x axis with respect to the y axis was estimated at ± 0.5 mm. A water vapor spray at the base of the tube was used to make the beams visible for photography. Double exposures were made: one of the beams in the tube center for reference and another at one of the selected off-axis positions.

The negatives of the photographs were examined on a Bausch & Lomb 10X optical comparator. Accuracy in the measurements of beam crossing position are estimated to be ± 0.4 mm, and of the probe volume rotation, ± 0.4 degrees. The accuracy was better at smaller off-axis positions.

The results of the experiment are tabulated with the calculated values at a number off-axis positions in Table V,for the case when $\beta_{1/2} = 5.15°$.Only this half angle was used for the measurements because an examination of the calculated results, tables I through IV, showed that the refraction effects were largest for this half angle. Off-axis distances do not have integer metric values because the translating table was calibrated in inches, and because small corrections in translated position were made using the reference

TABLE V

Comparison of Measured and Calculated Refraction Results
$\beta_{1/2} = 5.515°$

A. Horizontal beams

Off axis Position mm	y'_o mm		Δx mm		θ degrees	
	calc*	meas	calc*	meas	calc*	meas
5.50	5.50	5.4	-0.05	0.0	-0.48	-0.5
10.89	10.89	10.7	-0.21	-0.2	-1.10	-1.2
16.22	16.21	16.0	-0.62	-0.6	-2.17	-2.2
19.32	19.29	19.3	-1.16	-1.2	-3.39	-3.3
21.54	21.45	21.3	-1.92	-1.9	-5.04	-4.6
22.51	22.39	22.3	-2.49	-2.4	-6.25	-6.3
23.65	23.44	23.2	-3.60	-3.7	-8.62	-8.5
25.30	-	24.0	-	-5.8	-	-12.5

B. Vertical beams (y'_o and θ)

Off axis Position mm	y'_o mm		θ degrees	
	calc**	meas	calc**	meas
5.50	5.60	5.4	-0.55	-0.6
10.89	11.11	10.7	-1.25	-1.1
16.22	16.54	16.2	-2.46	-2.2
19.32	19.75	19.4	-3.84	-3.5
21.54	22.11	21.7	-5.67	-4.8
22.51	23.19	22.8	-7.09	-5.7
23.65	24.59	24.2	-9.79	-8.2

C. Vertical beams (Δx only)

Position mm	Δx mm	
	calc**	meas
0.00	-1.05	-1.1
5.36	-1.06	-1.1
10.71	-1.08	-1.1
19.29	-1.15	-1.2
21.43	-1.16	-1.2
22.51	-1.16	-1.0
23.57	-1.15	-1.1
24.64	-1.13	-1.0

* Linearly interpolated from table II

beams in the photographs. Because the camera was mounted in a different position to measure the x-value for the vertical beam intersection point, a separate set of off axis values were used and the off-axis positions were not exactly equal to those of the other tests.

2.4 Comparison of Predicted and Measured Refractive Effects

In all the measurements, as well as in the calculations, the intersection angle was essentially unchanged for both sets of beams. The majority of measurements agree with the predictions to within the accuracy of measurement. Small systematic discrepancies, probably due to errors in tube positioning, or to inhomogeneities in the tube, become pronounced only at large off-axis positions. Overall, out to 22.5 mm, the greatest discrepancies between calculations and measurements are only 1.4 degrees in rotation and 0.4 mm in position. The agreement for the horizontal beams is much better showing maximum differences of only 0.4 degree and 0.24 mm.

Beyond 22.5 mm, the larger disparities are possibly due to positioning errors, since the calculations show that in this region the probe volume position and rotation are very sensitive to position changes. Taking into account the work described above and the resulting agreement between analytic and experimental data, it can be assumed that the calculations can be used to accurately predict the position of the LDV beam intersection volumes. It should be noted that the rotation of the vertical beams through the angle θ does affect the fringe orientation by that amount while the rotation of the horizontal beams has no effect on the fringe orientation because the interference planes will remain horizontal.

III.

VELOCITY MEASUREMENTS USING THE LDV

3.1 Introduction

The purpose of this portion of the study is to simultaneously measure the radial and vertical velocity components of the transient flow velocity at points located on the tube axis during flame passage for upward propagation of a near-lean-limit flame in a standard flammability tube using a two color frequency shifted laser Doppler velocimeter. The apparatus, technique and results will be presented in some detail in this section.

Before describing the individual components of the experiment in detail, a brief overview of a typical experiment is in order. A standard flammability tube (SFLT) meeting the specifications of Coward and Jones [1] was filled from the top with a fuel/air mixture. The fuel and air flows were monitored by two separate rotometers and mixed just before entering the tube. The fuel went directly from the rotometer to the mixing point, whereas the air, after exiting the rotometer, went to a particle generator to collect seeding particles needed for LDV measurements. The tube was purged with a volume of mixture equal to ten times the volume of the tube. This ensures that the metered mixture composition is the actual composition in the tube. After filling, the SFLT was isolated and then opened at the bottom and ignited at the bottom using a hot-wire ignitor.

The gas velocities associated with the upward propagating flame were measured using a two watt, two-color, frequency-shifted LDV system. Frequency shifting permitted measurement of the flow reversal that occurred when the flame passed the point of measurement. Photodetectors in the system converted

the Doppler bursts to electrical signals of the same frequency, and these were fed into a Counter-type signal processor which converted each electrical signal to a voltage proportional to the signal frequency. The analog voltage output was recorded on a Tektronix Type 533A four channel oscilloscope. A referencing system was constructed to coordinate the time-dependent voltage with the changing position of the flame.

3.2 Flammability Apparatus

The flammability tube constructed for this study was copied from Levy[4] and is depicted schematically in Figure 22. It was constructed of 50.80 mm (2 in) ID, 3.175 mm (.125 in) thick clear plexiglass tubing, and was 1.8 m (70.9 in) in length, thus meeting the requirements specified by Coward and Jones.[1]

At each end of the tube a round plexiglass flange 24 cm in diameter was affixed eccentrically. The center of each flange served as the center of rotation for a plexiglass disk. The upper rotating disk (see Fig. 23) contained a plenum chamber where the air and methane used for filling the tube were introduced and mixed. There was also an open hole in the disk which could be positioned over the tube for venting and cleaning between tests. When neither of these two positions were used, the top end of the SFLT was in the closed position.

The rotating disk on the lower flange had a 7 mm diameter hole which was positioned under the tube to allow the gas mixture to flow out during the filling process (see Figure 24). After filling, the lower disk was rotated to the closed position for several minutes to allow the mixture time to become quiescent. It was then rotated to the open position for ignition. A heated nichrome wire was used as an ignitor.

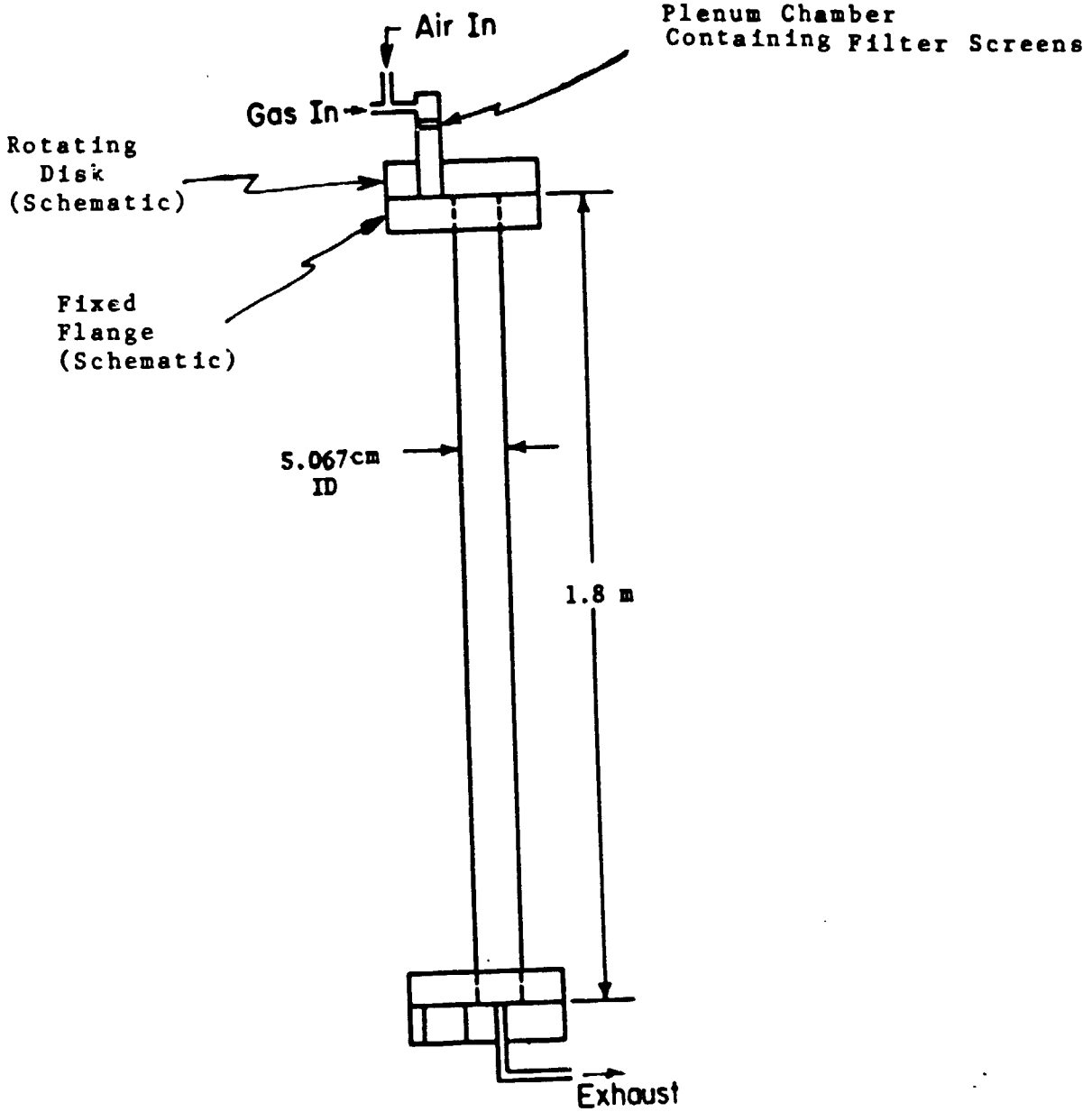

Figure 22 Standard flammability limit tube. (not to scale)

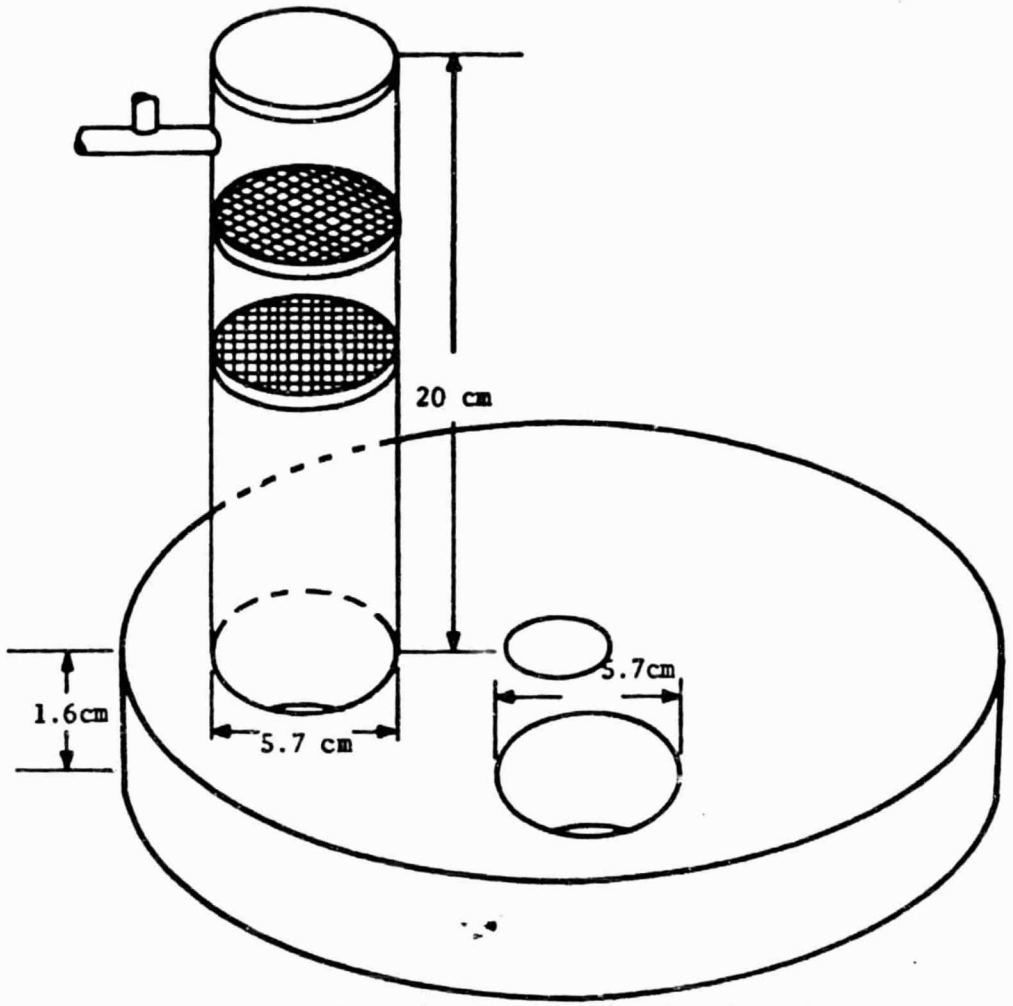

Figure 23. Upper rotary flange for introduction of gaseous mixture.

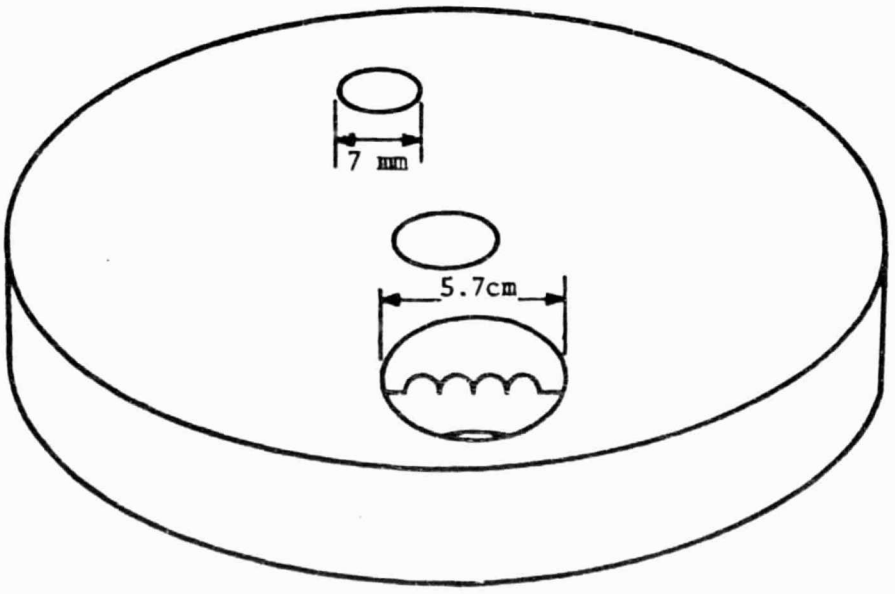

Figure 24. Lower rotary flange for draining and ignition.

3.3 The Combustible Mixture

The fuel used for this study was natural gas. This source was more readily available and much more inexpensive than bottled gas. An analysis of the gas is presented in Table VI. It was chosen because it is primarily methane and methane is the fuel of choice for the proposed space lab studies. Since the objective of this experiment was primarily the assessment of an experimental technique rather than the interpretation of the actual velocity measurements or the exact determination of a limit, there was no need to use pure methane.

The addition of small amounts of inerts to a flammable mixture has been shown by Jones and Kennedy[5] to have the same effect on the lean limit as the addition of air. Their measured values of flammability limits of mixtures of fuel were in excellent agreement with those predicted by Le'Chatelier's rule. Using values of the lean flammability limits from Coward and Jones[1], we will apply Le'Chatelier's rule to obtain the lean limit of the mixture. Thus,

$$\text{mixture lean limit, } L_m = 100/\left(\sum_{i=1}^{n} p_i / L_i\right)$$

$$= 100/(88.75/5.3 + 4.65/3.0 + 0.94/2.2 + 0.16/1.9 + 0.06/1.2 + 0.04/1.5)$$

$$= 5.30\ \%$$

The air and fuel were regulated using Matheson rotometers, model numbers 605 and 603, respectively. They were calibrated by measuring the time necessary at fixed rotameter settings to displace a known volume of water. The errors in calibration were estimated to be less than 3%. Errors in reading the rotometer settings were estimated at less than 2%, so an error no more than a 5% was expected.

The lean limit was first determined without the particle dispenser in the feed lines and found to be 5.04%. This is significantly lower than the value of 5.30% determined from Le Chatelier's rule. The analysis presented in Table VI, however, was 15 months old at the time of testing, so an increase in the percentage of ethane or propane might account for the lower limit observed. Nvertheless, the lean limit could be measured to an accuracy of at least ±.05%.

TABLE VI
Natural Gas Analysis*

Constituent	Volume Percentage	Lean Flammability Limit**
Methane	88.75	5.3
Nitrogen	4.88	Inert
Ethane	4.65	3.0
Propane	0.94	2.2
Carbon Dioxide	0.50	Inert
Butane	0.16	1.9
Hexane-Plus	0.06	1.2
Pentane	0.04	1.5
Helium	0.02	Inert
Hydrogen	tr	---
Oxygen	tr	---
Argon	tr	---
	100.00	

* Analysis from Illinois Power Company
** Values from Coward and Jones (1)

3.4 Particle Seeding for the LDV

A laser doppler velocimeter measures velocities of particles which are seeded in the flow. The requirements in this experiment were that the particles must: 1) accurately follow the flow; 2) scatter enough light to be detected; 3) be numerous enough to provide an adequate data rate; 4) keep their integrity in the hostile flame environment; and 5) absorb a minimum amount of heat. It is therefore desirable to use small but highly reflective

particles at a concentration as high as possible without significantly affecting the flame temperature.

Particle response to changes in fluid velocities is characterized by the particle relaxation time:

$$\tau = \rho_p d_p^2/18\mu$$

The particle velocity after a step change in fluid velocity (at a later time t) is then given by

$$v_p = v_f - (v_{f_o} - v_{p_o})e^{-t/\tau}$$

The particle settling velocity due to a balance between gravitational forces $(1/6\pi\ d_p^3\ g(\rho_p - \rho_f))$ and Stokes drag $(3\pi\ d_p\ \mu v_s)$ is

$$v_s = d_p^2\ g(\rho_p - \rho_f)/18\mu$$

Reuss [3] found aluminum oxide (Al_2O_3) particles are the best particles to use in a flammability tube. They are unaffected by the flame, have a specific gravity of 3.8, are roughly spherical, and are readily available from commercial suppliers in a variety of sizes from 0.1 microns to 40 microns. 0.1 micron diameter particles were used in Reuss's LDV system. Because aluminum oxide tends to cake it is impossible to generate a monodispersed powder of this diameter. The agglomerates formed from the particle generator were assumed to be less than 4 microns in diameter, so the relaxation time in the mixture at STP would be no more than 185 microseconds, and the settling velocity less than 1.8 mm/sec.

A particle generator constructed by Reuss, Figure 25, was used in this experiment with one alteration: approximately 5% of the lower chamber volume was filled with 2 mm diameter glass beads. Also a portion of the air flow entered the dispenser near its base and collected particles in the fluidized

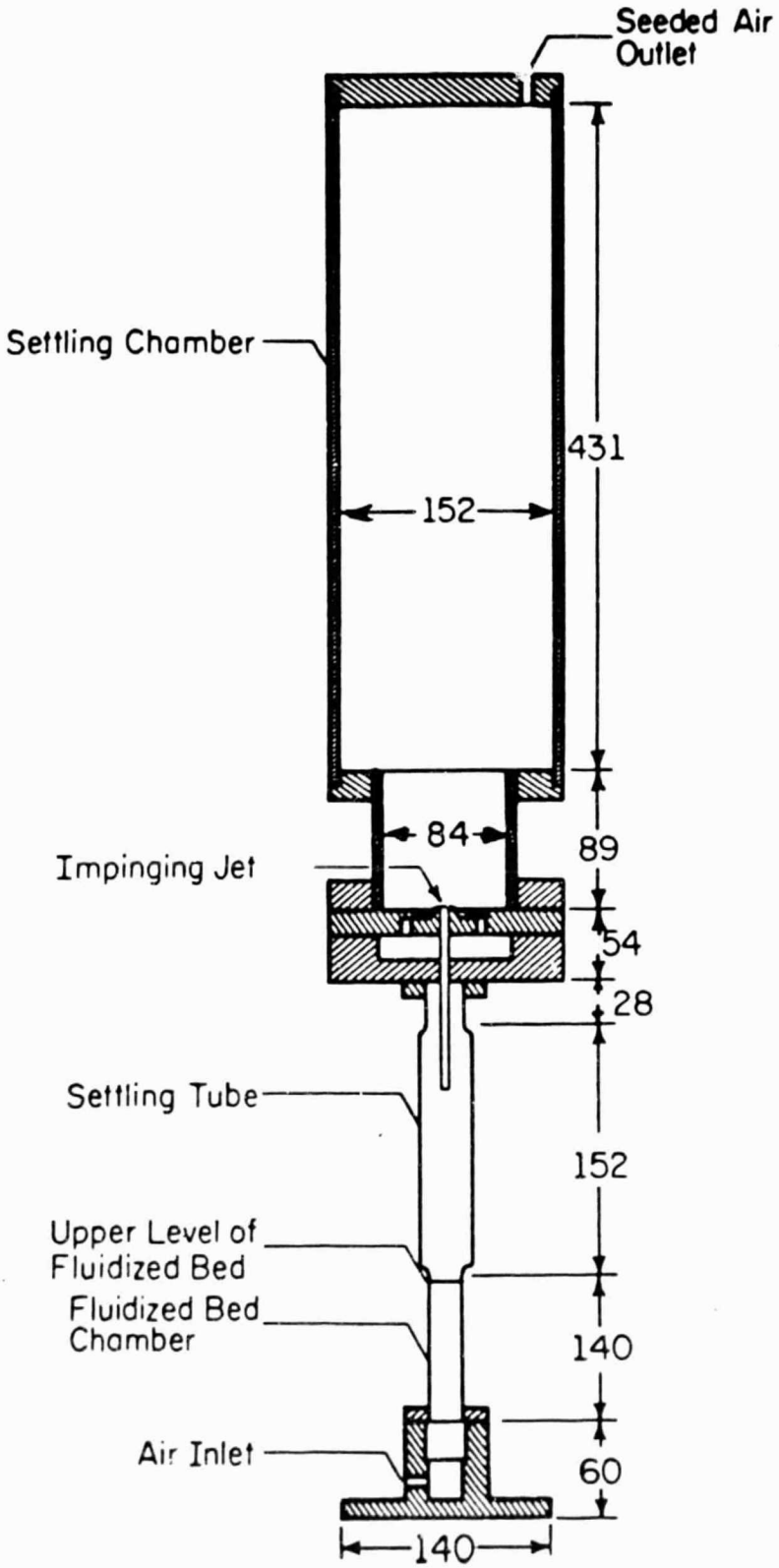

Figure 25 Aluminum oxide particle feed system. Dimensions in millimeters. Adapted from Reuss (18).

bed chamber. The air flow held the beads in swirling suspension, minimizing particle caking on the chamber walls. A 1.25 mm hypodermic needle with four opposing jets impinging at its termination limited the maximum agglomerate size when the flow left the fluidized bed chamber. After passing through a settling chamber, the particle laden air passed through the outlet at the top and was transferred via 6 mm plastic tubing to the mixing "T" at the top of the SFLT plenum. The particle generator caused a back pressure at the exit of the air rotameter of 20.7 kPa. The flow rate was adjusted by applying the relationship $\dot{V} = \dot{V}_m \sqrt{P/P_m}$.

There was no meter to measure the actual particle density. However, two observations can give clues as to the relative density. First, the particles present heat sinks to lower the flame temperature and thus raise the lean limit. The lean limit of the seeded mixture was measured as 5.07%, .03% higher than the unseeded limit. This difference is not entirely reliable, however, because it lies with the above mentioned error range of ± .05%. The second clue is the flame color. An unseeded flame has a dull violet color, while a highly seeded flame appears bright orange-yellow. The seeded flames observed in these experiments had a mixed violet and weak yellow color. This classification is, admittedly, very subjective; but it indicates that the flames were not highly seeded. The flame shape was not visibly altered by the presence of the particles, thus it was assumed that they were not significantly intrusive.

3.5 The Laser Doppler Velocimeter (LDV)

The SFLT and laser installation are shown mounted on a table with a translating platform in Figure 26. The table that the LDV is mounted on can be translated in two orthogonal directions and x, y. The (x, y) position of

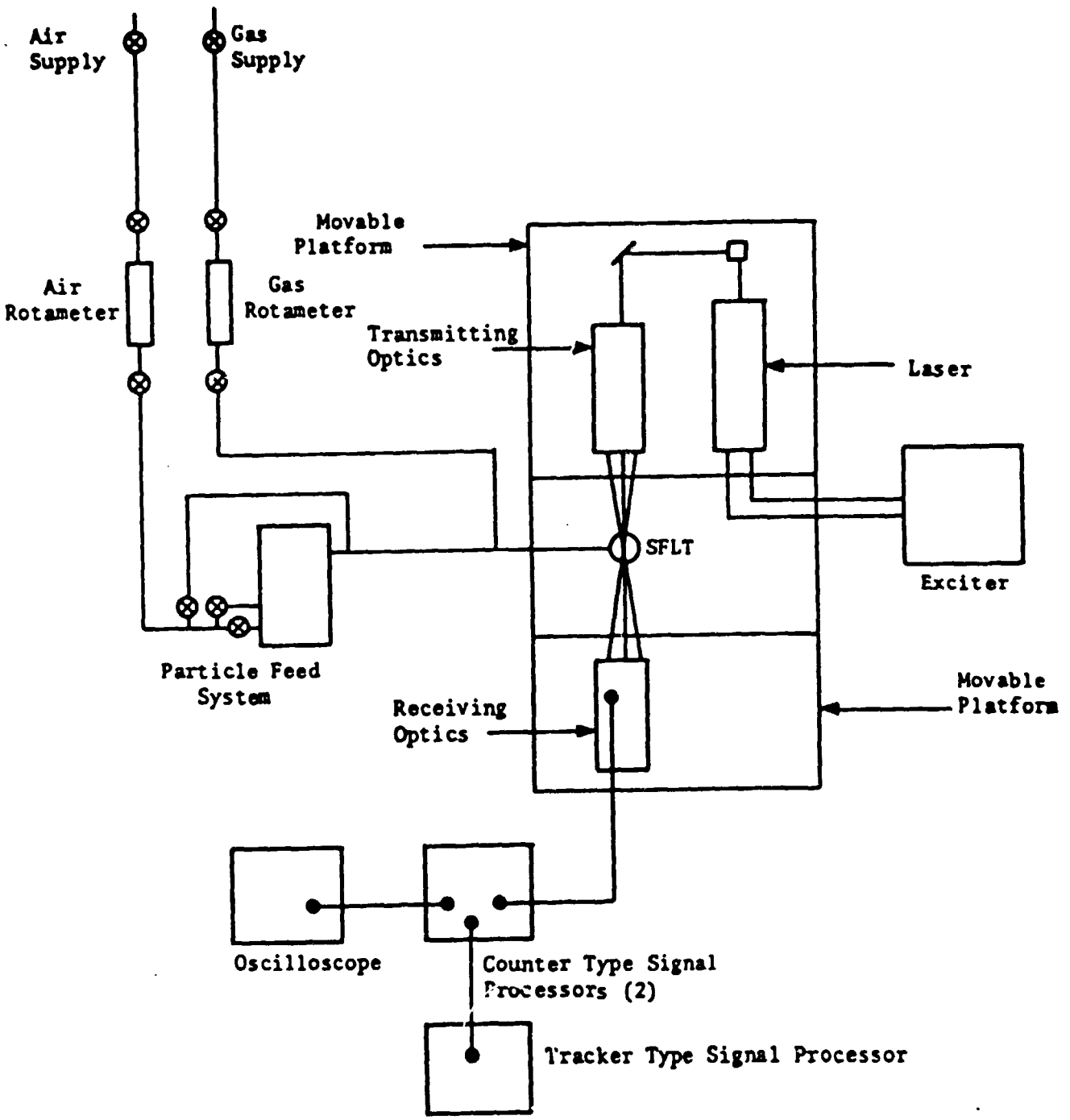

Figure 26 Overall arrangement of experimental apparatus. Referencing system is not included.

the measuring volume could be located in the SFLT to within ±0.001 inches.

Figure 27 depicts an LDV arrangement for forward scatter collection for clarity of illustration. In these experiments backscatter collection was used, and the receiving optics minus the receiving lens were mounted between the second Bragg cell and the transmitting lens. The transmitting lens then doubled as a receiving lens.

The laser was a Spectra-Physics Model 164-06 two watt argon-ion laser. It was powered by a Spectra-Physics Model 265 exciter. The exciter provided current to the plasma tube solenoid and controlled the ion discharge in the plasma tube so that a constant laser power output was maintained. The power of the two watt laser is highest at wavelengths of 488 nm (35% of total power) and 514.5 nm (40% of total power), corresponding to the colors blue and green, respectively. The beam leaving the laser was first collimated so that the probe volume fringes were parallel and so the beam "waist" or minimum diameter, would occur at the point of velocity measurement. The beam was resolved into its component colors by a TSI Model 901 dispersion prism. Plane mirrors directed the green beams down the main horizontal optical axis and the blue beams down a parallel axis to bypass the green beam splitter. The beam displacer realigned the blue beam along the main vertical optical axis. Polarization rotators were used to rotate the polarity of the beams perpendicular to the plane of the beamspiltter. In this way, the beams were resolved into two parallel components of equal intensity. The green beams were separated by 50 mm in the horizontal plane, and the blue beams by 50 mm in the vertical plane. Bragg cells were used to shift the frequency of one beam of each color and thus allow near zero and negative velocity measurements. They were powered by two TSI model 985 LDV frequency shifters, each with a shifting range of 10 KHz - 40 MHz. Three pairs of achromatic

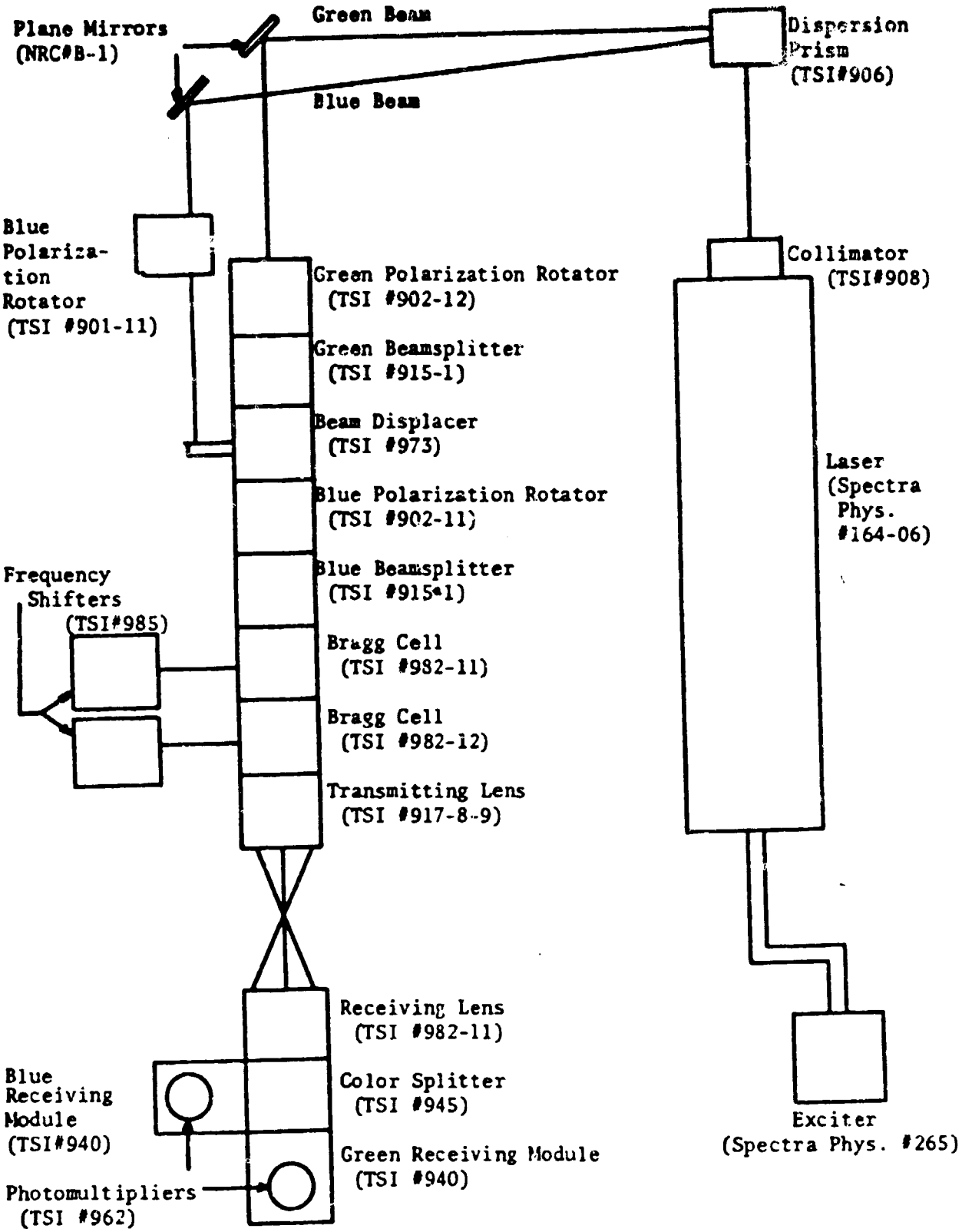

Figure 27. LDV assembly for forward scatter collection. (Note that while backscatter collection was used, a diagram of the forward scatter yields

lenses of focal lengths 120 mm, 250 mm, and 600 mm were available to focus the laser beams.

The constant of proportionality between the measured Doppler frequency and the flow velocity is the fringe spacing, d_f. The green beam fringe spacing for the 120 mm lens was determined by measuring the output frequency from a source of known velocity. A rotating disk was positioned so that the outer edge had a maximum downward velocity at the beam crossing. Tiny asparaties on the disk surface acted as particles to generate Doppler signals at a sufficiently high data rate. The disk diameter was measured as 22.02 ±01 cm, and the rotational speed was measured with a calibrated strobe as 1784 rpm ± 2 rpm. This implied an outer edge velocity of 20.57 m/sec ± 0.03 m/sec. The Doppler frequency was measured as 15.20 MHz, so the fringe spacing was simply calculated as $d_f = V_{wheel} / \nu_D = 20.574/15.20 \times 10^6 = 1.354 \times 10^{-6}$m ± $.003 \times 10^{-6}$m. This is within 1.5% of the manufacturer's specifications.

Beam collimation can be accomplished by making the fringes parallel. This was checked by translating the rotating disk along the long axis of the probe volume and adjusting the collimation until the frequency output (and thus the fringe spacing) was nearly constant. After final collimation, the fringe spacing varied by less than 0.8% across the probe volume where the data rate was at least $1/e^2$ (14%) of the maximum rate. The length of the probe volume as defined by the $1/e^2$ data rate positions was measured as 0.67 cm. This is of the same order of magnitude as the calculated value of 0.32 cm.

The receiving optics utilized a color splitter with a dichroic mirror to pass green light and reflect blue. The receiving modules focused the scattered light from the particles in the probe volume onto the photomultipliers. Each receiving module had a narrow band-pass filter; one passed only blue light, the other only green. This virtually eliminated noise

from other light sources such as the flame. TSI Model 962 photomultipliers were centered above each of the receiving modules. Clear apertures of 0.127 mm (.005 in) were centered between the photomultipliers and the receiving modules to block extraneous light not scattered from the probe volume. The photomultipliers each had a quantum efficiency of 22%, a sensitivity of 40,000 V/lumen, and a frequency response of 100 MHz. They converted any impinging light signal to an electric signal of the same frequency.

The output from each photomultiplier was directed to the respective frequency shifter for downmixing. With the 120 mm lens, the maximum frequency due to particles moving downward in the tube was approximately 0.6 MHz. The next highest frequency shift available was 1.0 MHz, so the green probe volume fringes were shifted downward at this value to maximize measurement sensitivity. Likewise, the maximum expected frequency due to radial velocities in the negative (outward) direction was 0.15 MHz, so the radial beams were shifted outward by 0.5 MHz. The frequency shifted outputs were transmitted to TSI Model 1990 Counter Type signal processors. They had high pass filters to eliminate the pedestal frequency, and low pass filters to reduce high frequency noise. The processors also rejected bursts which lacked a minimum number of cycles (from particles far from the probe volume center.) Best results for the measurement of vertical velocities were obtained with the filters set at 0.3 MHz and 2.0 MHz, and a minimum of 8 cycles per Doppler burst to be measured. For radial measurements, the filters were set at 0.3 MHz and 1.0 MHz, also with 8 cycles to be counted.

The counters produced an analog voltage proportional to the measured Doppler frequency. The voltage output was held until a new Doppler burst was encountered. The output when displayed on an oscilloscope therefore was a series of step functions. If the data rate was high enough, the output

approached a smooth curve. The proportionality constants of the counters, in V/MHz, were checked by inputting sine waves from a signal generator. The output was always within 0.4% of the expected voltage.

3.6 Referencing System

The output from the counter was a time-varying voltage proportional to the velocity at the point of measurement. It was necessary to reference the velocity with the changing position of the flame to make any meaning of the data. This was accomplished by determining the flame position at one instant of time and measuring the flame speed.

A Beam Deflection Flame Detector (BDFD) was copied from von Lavante[6]. The beam from a Spectra Physics model 124A 15 mWatt HeNe laser was split by a prism assembly into two parallel, horizontal components. The beams were directed through the tube center by making sure the beam reflections on the tube wall coincided with the beams themselves.

Two photodetectors (Motorola MRD 510-7727) were positioned to intercept the beams 1.7 m on the opposite side of the tube. The photodetectors were powered by a 5 volt DC power supply. In the absence of a flame, the laser beams struck the photodetectors, the circuits were completed, and a +5 volt deflection was registered on the oscilloscope. The density gradient associated with the preheat zone of the propagating flame first deflected the lower of the two beams and started an Industrial Timer Corp. digital clock (.001 sec resolution). The deflection of the upper beam stopped the clock. Single 1.2 mm apertures were placed in the beams on either side of the tube to increase the sensitivity of the system. The DC coupled output of the photodetector circuit was displayed on the oscilloscope to provide a temporal reference mark. The flame velocity was simply calculated by dividing the

measured distance between the two beams by the clock time.

The exact position of the visible flame with respect to the lower beam at the time the beam was refracted had to be determined photographically. It was also desirable to photograph the flame to determine its shape for use in a velocity profile construction. A Canon A-1 35 mm SRL camera was positioned facing the tube with the film plane parallel to the vertical plane formed by the two reference beams. When the flame deflected the lower beam, a voltage pulse was input into a Tekronix Type 555 oscilloscope. The oscilloscope was set for external triggering on a negative slope, so the voltage drop instantly triggered the oscilloscope and a +20 V gate pulse. The pulse opened a silicon control rectifier in a solenoid power circuit developed by Meagher[7] which activated a solenoid attached to the shutter release and exposed the film.

There was a mechanical delay from when the +20V gate pulse was initiated to the time of shutter opening. To determine this delay time, a calibration scheme developed by Reuss[3] was used. The lens of the Canon A-1 camera was removed and the camera back was opened. The beam from the 15 milliwatt laser was split by a prism into two parallel beams spaced 21.1 mm apart, and both beams were directed through the camera film plane. The beams struck photodetectors to complete two 5 Volt d.c. inputs to the oscilloscope. The shutter of the Canon A-1 consists of two shades which move from right to left when the camera is triggered. The first shade exposes the film as it moves, and the second shade covers the film. The movement of the first shade permitted the beams to pass through the camera body and complete the circuit.

To conduct the time delay tests, the oscilloscope was triggered manually, so that the sweep began at the same time the gate signal was triggered. During the time delay, the beam was blocked by the camera shades and the oscilloscope registered zero. The oscilloscope registered a step rise of 5

volts when the first shade uncovered the beams. The oscilloscope traces were photographed on Polaroid Type 667 film and are presented in Figure 27.

The results of these experiments indicated that the delay time was constant regardless of shutter speed. Photographs at every shutter speed from 1/125 sec to 15 sec showed a delay time of 73.3 msec ± 1.3 msec for the first shade to uncover half of the film plane. The shutter speed was measured as 3.1 m/sec, or 3.1 mm/msec.

A photograph of the particle-seeded flame is presented in Figure 28. The lower beam is the triggering beam, and the upper beam is from the two watt laser to provide vertical reference. Because the upper beam does not lie in the camera image plane, parallax effects make it appear slanted. However, it passes through the tube center, so the apparent beam separation along the tubeaxis served as the reference distance. The actual beam separation was 5.98 cm.

Five photographs were taken, and the negatives were examined on the Bausch & Lomb 10X optical comparator. Precise measurements were made difficult because of the ambiguity in the location of the flame's leading edge and the effect of smearing due to flame movement. During the exposure, the flame traveled (23.42 cm/sec) x 1/125 sec = 0.187 cm. The measured thickness of what appears to be the reaction zone (the relatively bright leading edge) is approximately 0.25 cm, but this may be in error because the upper edge is hard to define. However, near the center of the reaction zone, the luminescence is maximum and constant in the vertical direction before gradually fading in the upward direction. The leading edge of the visible flame at the time of shutter opening was assumed to be at the upper end of this zone of maximum brilliance. Because of the intensity decrease in either direction, it is safe to assume that the flames leading edge has been located

2V/Div.

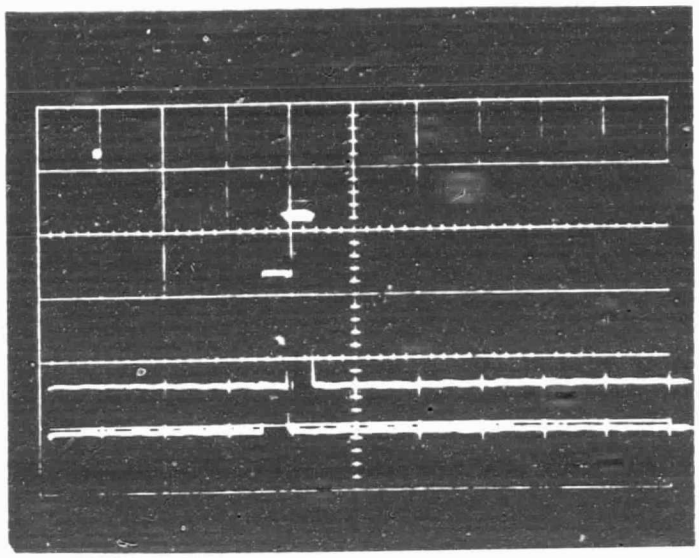

0.2 sec/div

2V/Div.

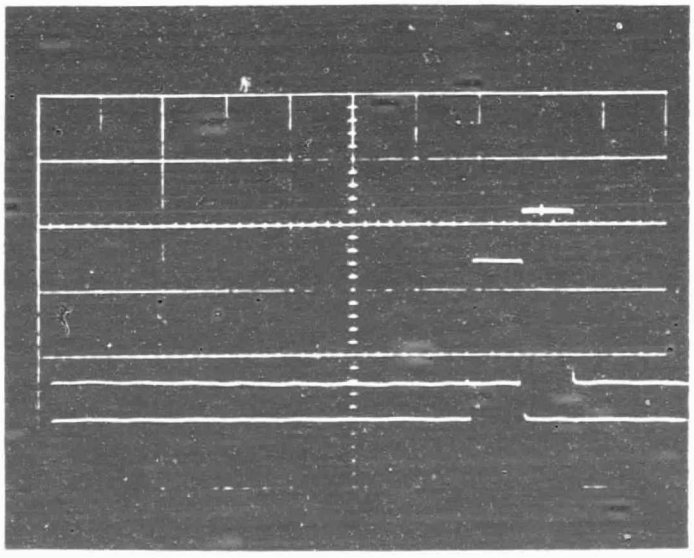

0.1 sec/div

Figure 27 Traces of camera shutter delay test.

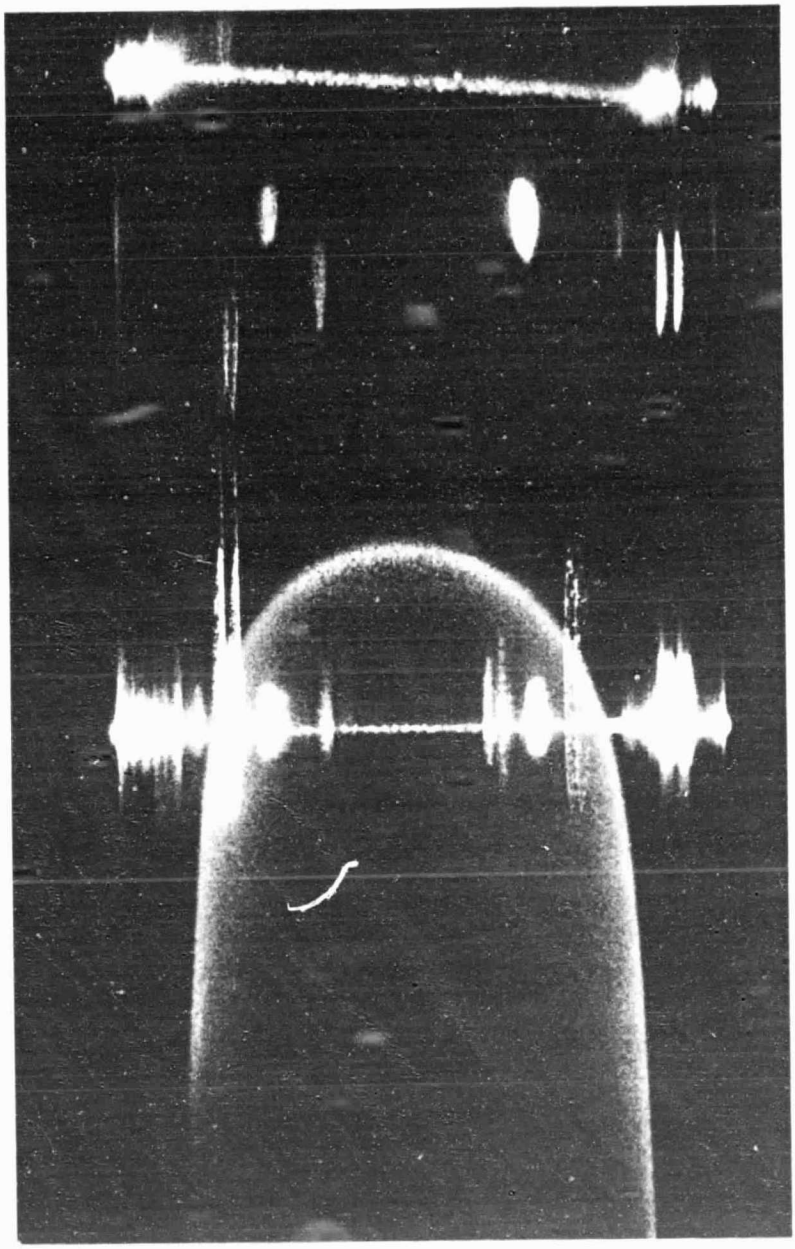

Figure 28. Photograph of a lean particle-seeded methane-air flame.

relative to the location of the Beam Deflection Flame Detector to within ± 0.15 cm. The refractive effects of the tube on the flame image were accounted for by photographing a grid placed in the tube at the camera focus. The results are tabulated in Table VII.

Three different photodetector aperture arrangements were used to determine if the aperture size had an effect on the time of beam deflection. The results, given in Table VIII, indicate that the beam is triggered slightly earlier when a larger aperture is used. This is surprising because it was assumed that the smaller aperture make the system more sensitive. However, not enough tests were performed to determine a reliable correlation. The combination of a 1.2 mm aperture on the entrance side and an 0.8 mm slit on the exit side was easiest to use, so it was decided that the visible flame tip

TABLE VII

MEASUREMENTS TO DETERMINE

REFRACTIVE EFFECTS OF TUBE ON FLAME IMAGE

r (true) (mm)	r (measured) (mm)
0.00	0.00
3.00	2.98
6.00	6.00
9.00	9.03
12.00	12.02
15.00	15.00
18.00	17.87
21.00	20.73
24.00	23.21

Tube internal radius = 25.335 mm

Measurement accuracy ± 0.03 mm

TABLE VIII

FLAME POSITION AT TIME OF BEAM DEFLECTION

AS A FUNCTION OF APERTURE ARRANGEMENT

Aperture - Tube Entrance Side	Aperture - Tube Exit Side	Distance of Flame Tip Below Beam
1.2 mm circular	1.2 mm circular	.203 cm
1.2 mm circular	1.2 mm circular	.215 cm
1.2 mm circular	0.8 mm slit	.108 cm
1.2 mm circular	0.8 mm slit	.096 cm
0.8 mm slit	0.8 mm slit	.064 cm

should be considered to be 0.10 cm below the lower triggering beam at the time of deflection.

3.6 Interfacing and Testing of System Components

Successful backscattering LDV measurements require first adapting the system to the given test conditions to produce best results. The output signal is optimized when the data rate and signal to noise ratio are miximized, and the data scatter (for laminar flow) is minimized. It was found that the quality of the signal was strongly dependent on the following: transmitting lens used, the laser power, photomultiplier alignment and particle concentration.

The calculated probe volume dimensions for the three lenses and green beam (514.5 nm) are shown below in Table IX.

TABLE IX

Probe volume diameter d_f and length l_m

for lenses with different focal lengths

Lens Focal Length	f	l_m
120 mm	.0605 mm	.317 mm
250 mm	.131 mm	1.30 mm
600 mm	.302 mm	7.36 mm

The 600 mm lens yielded a measuring volume much too large for these tests. It was originally felt that the 250 mm lens would be better suited than the 120 mm lens because the larger probe volume size would permit a lower seeding density to achieve the same data rate. However, the reverse was found to be true. The greatest source of noise is due to diffuse reflections off the tube wall caused by the beams striking the tube. With the shorter focal length lens, the bright spots on the wall were more widely separated, and the noise was reduced. This allowed the gain to be increased, thereby making a higher data rate possible.

The performances of the Tracker and Counter were compared. The analog voltage outputs were of the same quality for the measurement of radial velocities, but the Counter slightly outperformed the Tracker for vertical velocity measurements. The data rate was higher and the scatter was less. This was surprising, because a floating narrow bandpass filter normally makes the Tracker better adapted to noisy signals. On the other hand, the Tracker was easier to use because the data rate could be directly monitored. This was important for the alignment of the photomultipliers.

Photomultiplier alignment is the most critical factor involved in obtaining a good signal. By removing the photomultiplier, a TSI model 10096 eyepiece was placed over the receiving module for focusing and rough

alignment. When scattered reflections from the tube were observed to cross over the probe volume, the signal was later observed to be noisy. Reflective interference was serious for both the vertical and horizontal beams at r < 5 mm and r < 20 mm. In these ranges, it was found advantageous, especially for radial measurements, to set the receiving modules slightly out of focus so that the reflected images lay outside the 0.127 mm diameter area of the photomultiplier aperture. This compromise resulted in a significantly increased data rate and signal to noise ratio.

Frequency shifting caused the particles that were settling in the tube before the combustion tests to generate a Doppler signal. This permitted photomultiplier alignment by finding a peak in the data rate and signal to noise ratio. The signal to noise ratio for these purposes was defined as the normal data rate divided by the data rate obtained when one beam was blocked. Between r = 5 mm and r = 20 mm, the signal to noise ratio was always at least ten.

An indication of the accessibility of the LDV at different axial positions is the relative data rate obtained during the particle settling stage. The data rates from the horizontal and vertical beams were measured as a function of radial position, and showed a large dropoff when r exceeded 20 mm. Horizontal measurements at any given radius were more susceptible to reflective interference than vertical measurements, and were made difficult or impossible at r < 3 mm and r > 22 mm. Vertical measurements were possible at all axial positions, but were more difficult in the same two regions.

For reasons unexplained, the blue beams yielded a poor signal compared to the green beams for velocity measurements. In an effort to obtain the best possible performance, the green beams were used to measure both the vertical and radial components. The problem was certainly due to the particular LDV

system being used, and in no way suggests that simultaneous data could not be collected by a different LDV system.

The only obstacle to simultaneous data collection is the fact that the two probe volumes are not coincident. Refractive effects of the tube on the radial and vertical probe volumes cause this problem (see Tables I-V). The differences in the y-positions of the two measuring volumes is tolerable at all axial positions except very near the tube wall. On the other hand, the x-positions always differ from each other by approximately 1 mm. The horizontal beams can be "forced" to intersect near the vertical beams by passing them through a glass plate before striking the tube. The shift in the probe volume location is approximately 1/3 the glass thickness in the minus x direction.

This method was tested and determined to be viable if the glass plate can be oriented parallel to the transmitting lens to within two or three degrees. Gross misalignment causes refraction errors which are greater than the attempted probe volume shift.

The beams can quite easily be located in the probe volume center with high precision. The transmitting optics were first translated in the y direction until all secondary beam reflections formed a symmetric pattern on the tube wall. This located the probe volume on the x axis to an accuracy of ± 0.06 mm in the y direction. The table was then translated in the positive and negative x directions until the converging beams formed a single spot on the front and back inside walls. The table positions were measured with metric dial gages, and the probe volume center was assumed to be located exactly midway between the two readings. Accuracy of centering the probe volume on the x axis with respect to the y axis was estimated at ± 0.5 mm.

3.7 Experimental Procedure and Results

It has been observed by Reuss[3] and others that the speed at which a near lean-limit flame propagates up an SFLT increases with test number if the tube is not cleaned between runs. The problem can be eliminated by cleansing the tube wall with water after every run. In these tests, the tube walls were first wiped with dry chamois to remove any particles clinging due to electrostatic charges. The tube was then washed with a water filled sponge. It is important in the drying procedure to generate as small a static charge as possible on the walls to prevent seed particles from clinging to the walls during the tube filling process. Drying the tube entirely with an air flow is much too slow a process. Instead, the tube was partially dried with a cotton cloth, and then totally dried with an air jet. The experimental procedure for a test cycle is given in Table X.

3.8 Experimental Results

Tests were run on a 5.27% mixture flame for vertical velocities at r = 0, 5, 10, 15, 18, 20, 22, and 23.5 mm, and for radial velocities at r = 5, 10, 15, 18, 20, and 22 mm. At least two tests were performed at each station to determine repeatability. Tests were also performed on a 5.51% mixture for vertical velocities at r = 10 and 18 mm. Only one test was made at each location for these latter runs.

The raw data from the 5.27% tests is presented in Appendix C. It represents the data which was most closely repeated in comparison tests, and for which the flame was observed to be not significantly asymmetric. On the figures in Appendix C, the upper straight line is a zero velocity reference, representing the voltage corresponding to the amount of frequency shifting. The lower straight but broken line is the d.c. coupled output of the beam deflection flame detector. The voltage jump begins when the flame deflects

the lower reference beam, and ends when the upper beam is deflected. The beam separation was 11.30 cm. The probe volume was located at the same height as the lower beam, so the uppermost tip of the flame was 0.10 cm below the probe volume at the time of this deflection.

TABLE X

EXPERIMENTAL PROCEDURE

- Fill tube with particle laden mixture for 150 sec
- Close top and bottom flanges simultaneously
- Align photomultipliers
- Adjust gain for reasonable data rate
- Align beam deflection flame detector
- Open bottom flange and ignite with hot wire
- Start oscilloscope trace when flame is 0.1 m below probe volume
- Photograph reference trace for zero velocity
- Vent tube
- Remove particles from tube wall with dry chamois
- Wash tube with water filled sponge
- Partially dry tube with cotton cloth
- Dry tube completely with air jet

The traces presented in Appendix C were analyzed with a Hewlett Packard model 9864A Digitizer. The two voltage scales of the oscilloscope were calibrated, and two third order polynomials were determined to account for scale nonlinearity. A program was written to convert the voltage data directly to velocities with respect to a flame of average propagation speed.

The average flame velocity of the 5.27% mixture was 22.89 cm/sec with a standard deviation of 0.55 cm/sec, and that of the 5.51% mixture, 23.80 cm/sec, with a standard deviation of 0.45 cm/sec.

The reduced data is presented in Tables XI through XIII. It was obtained by first curve-fitting the output data from the digitizer, then measuring velocities from the curves at regular intervals. Vertical velocities for the 5.27% mixture at r = 0, 5, 10, 18, 20, and 23.5 mm are the average of two separate tests. z=0 is defined at the uppermost tip of the flame. The shape of the flame was measured on the optical comparator for use in the velocity profile construction. A composite of two symmetric flames is drawn in Figure 29, with velocity vectors drawn in a coordinate system which moves with the flame. Refer to the photograph of Figure 28 for comparison to the actual flame.

The accuracy of velocity measurements is largely dependent on the scatter of data. The experimental scattter in this investigation was usually no more than ± 1.6 cm/sec for vertical velocities and ± 0.9 cm/sec for radial velocities. Since turbulence is assumed to be absent, a mean curve is considered to represent the true velocity. Ambiguity of the placement of the mean curve was approximately one half the maximum data scatter, so the measurement accuracy was extimated at ± 0.8 cm/sec for vertical velocities, and ± 0.45 cm/sec for radial velocities.

Vertical velocity measurements are possible at all axial positions, but the signal is degraded by reflective interference at r<3 mm and r>22mm. Radial velocity measurements are possible in the region 3 mm <r< 22mm.

Signal dropout was found to occur in radial velocity measurements at r = 18 mm during flow reversal. This may be due to the beams becoming temporarily uncrossed or to a particle density gradient near the flame zone. It is not unreasonable, however, to interpolate on the range where the data points are sparse.

	POSITION ON Y-AXIS (MM)							
Z(cm)	0.0	5.0	10.0	15.0	18.0	20.0	22.0	23.5
-5	23.9	23.3	24.8	23.8	23.8	22.1	23.8	23.6
-4	23.8	23.0	24.2	23.8	23.8	22.2	23.8	23.6
-2	23.8	22.6	23.6	23.3	23.5	21.8	23.5	23.3
-2	22.5	21.9	23.1	22.0	22.2	22.3	23.7	23.0
-1	20.2	20.9	20.8	21.5	22.7	25.2	26.9	24.8
0	15.9	17.4	15.0	25.0	26.0	28.7	30.5	28.3
1	11.2	17.6	26.5	32.1	34.9	35.8	37.7	43.3
2	13.3	27.9	38.5	45.6	49.6	49.4	51.3	56.4
3	17.1	38.6	47.0	57.2	64.4	64.1	64.4	65.4
4	32.7	54.8	59.6	70.8	78.9	74.9	77.5	74.3
5	43.0	70.3	72.3	81.8	90.0	82.2	85.3	80.2
6	51.2	84.5	89.1	94.3	101.7	89.0	93.0	84.8
7	61.0	95.0	97.8	107.4	114.0	95.5	98.5	86.8
8	67.5	103.4	103.4	113.4	117.5	100.6	99.1	85.7
9	73.3	109.6	107.3	118.1	115.8	103.8	97.2	81.7
10	77.8	110.8	108.1	111.7	111.6	104.1	90.2	78.4
15	88.3	95.2	96.4	89.4	78.1	89.0	70.9	62.1
20	80.6	74.1	73.2	69.5	63.6	69.7	68.0	55.2
25	61.7	56.3	54.3	55.9	60.4	59.8	67.9	53.6
30	34.8	39.8	39.4	48.6	61.7	57.8	69.1	53.8

Table XI Reduced vertical velocity data for 5.27% mixture. Velocities are in cm/sec, positive downward, relative to upward traveling flame of V_p = 22.89 cm/sec. Z is vertical position in tube, positive downward, referenced from flame tip.

	POSITION ON Y-AXIS (MM)					
Z (cm)	5.0	10.0	15.0	18.0	20.0	22.0
-5	-0.1	0.0	0.0	0.0	0.0	0.0
-4	-0.2	0.0	0.0	-0.1	0.0	0.0
-3	-0.2	0.0	0.0	-0.3	0.0	0.0
-2	-0.8	-0.3	0.0	-0.6	-0.4	0.0
-1	-2.7	-2.2	-2.5	-0.8	-1.1	0.0
0	-8.7	-8.1	-6.0	-3.3	-2.1	0.0
1	-3.4	-16.2	-12.5	-11.3	-4.1	-0.1
2	0.7	0.4	-3.3	0.7	-8.3	-0.4
3	2.4	4.1	5.8	12.6	-5.0	-1.3
4	3.7	6.2	8.6	15.6	0.3	-2.3
5	4.9	7.3	10.3	16.5	4.2	0.3
6	5.7	8.7	11.1	17.5	7.3	4.1
7	6.3	9.6	12.3	15.8	10.8	6.7
8	6.8	10.3	12.7	8.3	14.1	9.9
9	7.1	10.5	12.5	2.2	13.5	9.3
10	7.2	9.9	11.5	0.3	9.8	3.4
15	5.0	3.6	2.3	-1.5	-1.5	-1.3
20	1.9	0.8	-0.7	-1.4	-1.6	-1.0
25	0.6	-0.4	-1.5	-1.3	-1.7	-0.8
30	0.4	-1.0	-2.0	-1.3	-1.8	-0.6

Table XI I Reduced radial velocity data for 5.27% mixture. Velocities are in cm/sec, positive radially inward. Z is vertical position in tube, positive downward, referenced from flame tip.

POSITION OF Y-AXIS (MM)

	Vertical Velocities			Radial Velocities	
Z (cm)	0.0	10.0	18.0	10.0	18.0
-5	22.8	26.5	25.0	0.0	0.0
-4	22.8	26.5	24.8	0.0	0.0
-3	22.8	26.5	22.8	0.0	0.0
-2	21.3	26.2	22.2	-0.7	0.0
-1	17.2	22.4	24.6	-4.0	-0.9
0	11.1	23.5	28.1	-8.0	-3.5
1	21.7	32.3	37.3	-14.3	-8.6
2	30.4	43.2	56.8	2.8	-3.0
3	38.3	54.8	69.8	9.7	11.0
4	49.3	74.0	81.9	12.4	13.7
5	59.5	83.9	90.1	13.6	14.6
6	69.0	92.7	99.0	14.0	14.0
7	78.8	100.1	106.6	13.8	12.0
8	86.0	105.4	110.2	12.3	8.3
9	91.0	111.4	112.2	8.1	2.6
10	94.1	113.9	110.8	3.6	0.8
15	94.8	103.8	84.9	0.6	-0.7
20	83.7	85.3	69.5	-0.3	-0.7
25	58.9	57.2	63.1	-1.0	-0.7
30	27.7	31.1	60.2	-1.5	-0.7

Table XII I Velocity data for 5.51% mixture. Velocities are in cm/sec. Vertical velocity is positive downward, relative to upward traveling flame of V_p = 23.80 cm/sec. Radial velocity is positive radially inward. Z is vertical position in tube, positive downward referenced from flame tip.

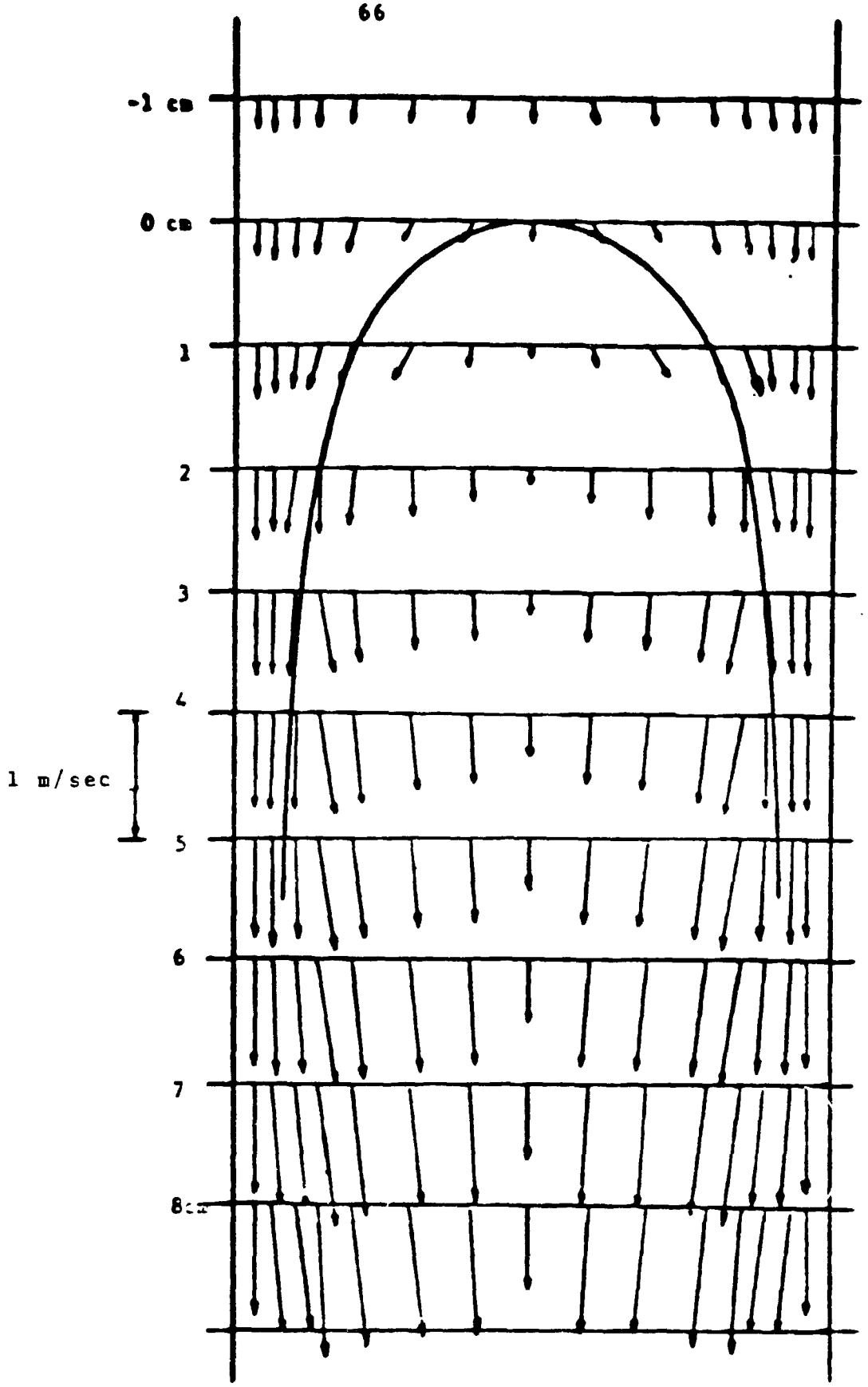

Figure 29. Gas velocities in a coordinate system that is moving with the flame. No radial velocity information was obtained at r = 23.5 mm. The lengths and direction of the arrows represent local velocity and direction of the flow at the point where the vector originates. The scale is represented by the vector length on the left side of the figure.

IV

INTERRUPTED PARTICLE-TRACKING (AN ALTERNATE METHOD)

4.1 Introduction

It was shown in Section 2 that the refractive effects of the curved tube walls have a deleterious effect on the position of the LDV intersection volume. To avoid these problems, an interrupted particle-tracking technique was considered as an alternate means of measurement. Particle-tracking was assessed as being feasible because it was known to have some advantages over LDV. For instance, particle-tracking allows velocity measurements at all off-axis positions in a single experimental run.

The basic theory behind interrupted particle-tracking is quite simple. As in LDV, the goal is to measure velocities of minute particles which are seeded in the flow. The particles are illuminated by a high intensity light source which is interrupted at a fixed frequency for a fixed fraction of time. In this way, a moving particle appears on a photograph as a series of short streaks. By knowing the frequency and interruption fraction and by measuring the distances between and length of successive streaks, particle velocities may be determined.

4.2 Experimental Arrangement

In this study, the two watt laser again served as the light source. To measure vertical and radial velocity components, a vertical plane which bisects the tube and is perpendicular to the viewing axis of a photographic camera was illuminated by a vertical plane of laser light. Such a vertical plane of laser light was produced by directing the laser beam through a horizontally mounted circular glass rod, as depicted in Fig. 30. The rod spreads the light so that a vertical plane of light is formed which passes

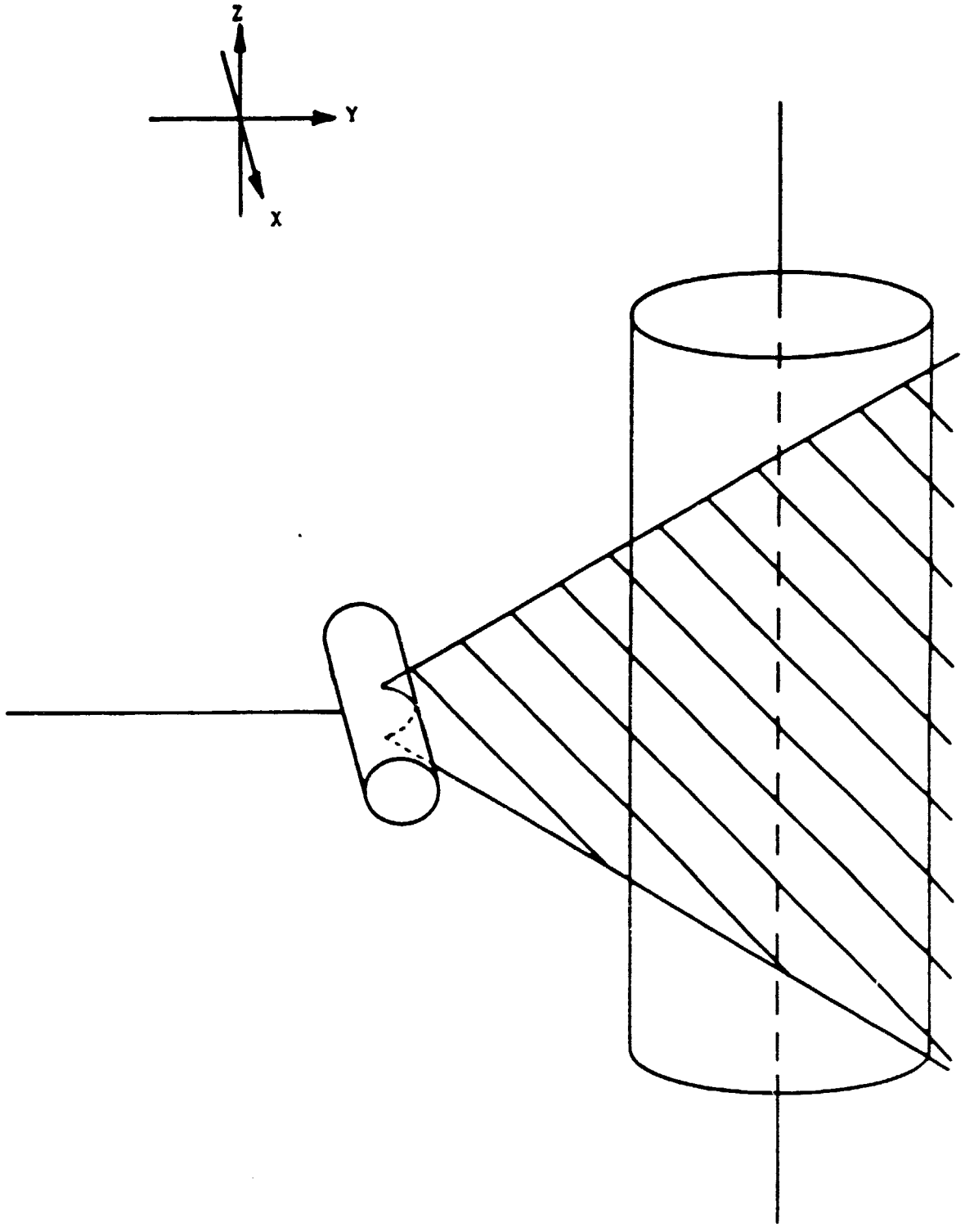

Figure 30 Circular glass rod is parallel to X-axis and spreads laser light in a Y-Z plane through the tube main axis.

through the tube. To produce a strobe effect, a rotating toothed wheel was placed in the path of the laser beam ahead of the glass rod. The illumination frequency could be varied by changing the number of teeth on the wheel or its rotational speed.

A Canon A-1 camera was positioned facing the tube so that the film plane was parallel to the plane of light illuminating the particles, and was focused on this plane. Alignment of the camera film plane and the light plane was accomplished in ways similar to those described in section 2. The photodetector circuitry used in the LDV study to create a reference time mark was used in these tests to trigger the camera automatically. Details of the triggering system are given in section 3.5. When the flame deflected the lower beam, there was a 73.3 msec delay to the time of shutter opening.

4.3 Photographic Limitations and Optimization

A photograph of the particles during flame passage showed many different series of streaks, but no flame image since the flame swept across the field during the exposure. The flame position at the time of shutter opening was determined by measuring the flame speed and referencing the flame with respect to the lower triggering beam by applying the shutter delay time. It was important to identify the first streak of every particle and assign it a time t=0. There is an error that has a maximum value equal to the time when the particles are not illuminated, since the particles might not have been illuminated at the time of shutter opening. To ensure that most particle trails started within the photographed region, the exposure needed to be 1/15 sec or less. Otherwise, most particles were observed to enter the photograph at one edge and leave at another, leaving no clue as to the time of passage.

Such short exposures required a set of photographs to record the entire velocity history of the flame passage, and hence defeated one goal, that of obtaining all velocity data from a single flame.

A related problem was encountered by Levy[4]. He attempted to use the flame itself as reference by limiting his exposure to 1/100 sec. However, the particles barely moved during such a short exposure, and little information could be obtained. With longer exposures, the flame image was smeared, and referencing was impossible.

It was necessary to find a combination of particles and photographic system which would yield clear images of particle streaks. The aluminum oxide particles used for LDV experiments were highly reflective and were considered the best suited for these experiments. To determine the best photographic system, tests were conducted by filling the tube with particle laden air and photographing the particles under strobe illumination. It was immediately observed that a portion of the laser light that was used to illuminate the particles also remained in the tube walls because of internal reflection. This portion of the light that was reflected inside the tube when the light sheet first struck the tube, and again when it exited the tube eventually was radiated from the tube and obscured particles at off-axis positions greater than 60% of the tube radius.

This problem can be alleviated by passing the light sheet through a 0.8 mm wide slit before it enters the tube. The slit helps to shield the tube from scattered laser light from the dispersed beam so that the tube is illuminated only be light which is needed for particle illumination. This allowed particle to be seen at off-axis positions up to 70% of the tube radius.

In the determination of the optimum photographic system, there were three

parameters which had to be determined: the camera lens system, the film, and the developer. Since it was desired to use particles as small as possible to follow the flow and minimize heat absorption, a fast photographic system is required. Four lens systems for close-up work using the Canon A-1 were tried, and are listed here in order of greatest speed: 1) Canon 50 mm f1.8 lens with 20 mm extension tube; 2) Vivitar f2.8 macro lens; 3) Vivitar 210 mm telephoto lens with Vivitar #2 close-up lens; and 4) the Canon 50 mm f1.8 lens mounted in tandem with a 12 mm extension tube and a Vivitar 2x teleconverter. Four different film/developer combinations were tested and are listed here in order of greatest speed and resolution: 1) Kodak Recording Film 2475 (ASA 1000), Kodak DK-50 developer; 2) Kodak Tri-X pan film (ASA 400), Optimate-2 developer; 3) Kodak Tri-X Pan film, (ASA 400), Kodak Microdol-X developer, and; 4) Kodak Plus-X film (ASA 100), Kodak Microdol-X developer. When using the f1.8 lens and 20 mm extension tube with Kodak Recording Film 2475, aluminum oxide particles as small as 3 microns in diameter (assuming no agglomeration) were identifiable in photographs of the upward propagating flame.

Although 3 micron diameter particles could be detected, contrast between the particles and the internal reflections was not enough to permit reliable identification at different time periods. Particles as large as 9 microns diameter were necessary for sufficient contrast, although further refinements in experimental technique would have certainly lowered this minimum size. Since traces of the smaller particles were difficult to distinguish, positive identification of the same particle after an interruption of the beam had occurred was sometimes dubious. This made velocity determination using this technique a tedious and time-consuming task.

The 15 mW laser was tested against the 2 W laser as the light source in order to predict the performance of the Spacelab laser. The results obtained using the two lasers were comparable. The particles were not as well illuminated by the smaller laser, but the tube luminescence was also diminished, so that the contrast between the particles and tube was about the same.

Finally, scales should be placed on either side of the tube in the same plane as the sheet of laser light after flame passage and photographed as a double exposure to provide a scale for the measurements. Particle-tracking tests were terminated before this step was implemented.

4.4 Appraisal of Interrupted Particle-Tracking

The four main advantages of LDV over particle-tracking are: 1) smaller particles may be used; 2) velocity data at greater off-axis positions may be obtained; 3) data acquisition and velocity determination are less tedious, and; 4) most importantly the interpretation of each interrupted trace on a photographic record is difficult, and it would be particularly difficult to determine the exact relationship between particle position and flame motion. Thus, particle-tracking as applied to flammability tube work is probably not feasible because it is more vulnerable to error and misinterpretation than originally anticipated and it should not be investigated further.

V

PREDICTED PERFORMANCE OF A 25 mW SYSTEM

Power limitations on Spacelab require the use of a 15 mW (nominal) laser. A new 15 mW He-NE laser emits 25 mW at λ = 632.8 nm. Two component measurements must be made by means of polarization separation. A 15 mW air cooled Argon ion laser emits 9 mW at λ = 514.5 nm, and 15 mW at λ = 488.0

nm, so that color separation can be used to resolve the two components.

The following analysis is based on a two color Argon ion laser. It should be noted that a He-NE laser may be preferred because the entire output power is concentrated at one wavelength. This is an advantage when making one-component measurements, such as on the tube axis.

Ref. 8 defines the signal to noise ratio as

$$SNR = 4X10^{11}\left(\frac{\eta_q P_o}{\Delta f}\right)\left[\frac{D_a d_e^{-2}}{r_a f}\right]^2 d_p^2 G\, V^2$$

For identical testing conditions, η_q, d_p, Δf , and f are equal. D_a/r_a is assumed to be equal to 1 if a 120 mm collecting lens is used. From Adrian and Fingerson (1) visibility V is dependent primarily on the ratio d_p/d_f, so V should also be equal. Then, $SNR \sim P_o G d_e^{-2}$. The vertical velocity measurements made in this experiment required a maximum of 0.24W in each beam, and only 0.17W per beam in the range 5 mm <r< 22mm. Assuming the 514.5 nm beams are to be used to measure vertical velocities, the power required to obtain the same SNR achieved in these tests is:

$$P_{o)_{.015}} = P_{o)_{2.0}}\left[\frac{G_{BS}}{G_{FS}}\right]\left[\frac{d_e^{-2})_{2.0}}{d_e^{-2})_{.015}}\right]^2$$

No information was found in the literature on the scattering parameters of Al_2O_3 as a function of collection angle. The particles are not truly spherical, and Mie scattering theory may not accurately apply. However, since the ratio d_p/d_f is estimated to be on the order of 3, the ratio G_{BS}/G_{FS} should be quite small,[9] and an estimate of 1/100 is considered conservative. In that case,

$$P_{o)_{.015}} = 0.24W \frac{1}{100} \left[\frac{1.30}{0.63}\right]^2$$

= 10.2 mW required in each beam, or 20.4 mW total. A similar analysis for the blue beams indicates a requirment of 25.4 mW at λ = 488.0 nm. The above analysis is intended only for an order of magnitude estimate, and indicates that a 15 mW laser operating in forward scatter might possibly achieve the same SNR obtained with the 2 W system in backscatter. A more sophisticated prediction for the expected performance can be computed by a program written by Meyers[10], at NASA Langley, which is available at NASA Lewis.

It should be mentioned that any calculation of relative performance may be significantly inaccurate. For instance, it is difficult to predict the reduction in reflective noise attained by off-axis positioning of the collection optics, or the scattering parameters of Al_2O_3 as a function of collection angle. Perhaps the most reliable method is to compare the vertical velocity measurements of this experiment to those obtained by Reuss with a 15 mW system and use the comparison to predict the performance of the smaller laser in radial measurements.

Reuss measured the vertical velocities in a glass tube with forward scatter collection to an accuracy of $\pm$0.5 cm/sec, as compared to $\pm$ 0.8 cm/sec attained in this experiment. There is reason to believe that Reuss' particle concentration was higher, since the particle presence raised the lean limit from 5.27% to 5.37%, a 0.10% increase, versus the 0.03% increase observed here. The higher data rate would allow the gain to be reduced, resulting in a greater SNR and less scatter. It is therefore assumed that the two systems would yield similar results under identical testing conditions. Reuss'

attempts to measure radial velocities were hindered by signal dropout for much of the time. He attributed this to the beams becoming uncrossed. However, beam deflection should only occur for a short time near the reaction zone, where density gradients are most severe. Moreover, the radial measurements made in this experiment did not exhibit prolonged dropout. Reuss' system was not equipped with frequency shifting, and the Tracker most probably lost the signal when the velocity was below 5 cm/sec. The radial velocities were found here to be below this value for most of the time. His data did show a sharp velocity peak near t=0 of about 13 cm/sec, and another more gradual peak near t=0.2 sec of approximately 10 cm/sec. This is consistent with the results obtained here, and indicates that it was the absence of frequency shifting, not beam deflection, which prohibited radial measurements.

Based on the above comparisons, it is concluded that a 15 mW frequency shifted two component LDV system operating in forward scatter should achieve similar performance to the system used here. There is also the possibility of superior performance through optimal positioning of the collection optics and transducers.

VI

RESULTS AND CONCLUSIONS

As was mentioned in the introduction, the purpose of this study was to: 1) calculate and verify by experimental measurement the effect of the presence of the circular walls of an SFLT on the location and rotation of the fringe patterns of an LDV, 2) measure the radial and vertical components of the velocity vector during flame passage, 3) investigate the feasibility of using an interrupted particle track technique to follow the flow associated with flame passage and 4) assess the feasibility of using a 25MW LDV in the

Shuttle or Space Lab to determine the flow velocity field associated with the passage of the flame under zero g conditions.

All of these tasks have been accomplished. The comparison of the calculated and measured location and orientation of the LDV measurement volume is quite satisfactory and shows that one can determine the deflection caused by the circular tube walls using simple ray tracing techniques. The flow associated with flame passage for upward propagation of a near limit flame in an SFLT in the earth's gravity field has been measured. The use of the interrupted particle track technique for investigating the flow associated with the passage of a transient flame in SFLT has been evaluated and found to be inferior to the LDV method. Thus, in this report, it is recommended that this technique should not be considered again. Finally an evaluation of the feasibility of using a 25 mW LDV for transient flow velocity measurements in either the Shuttle or Space Lab leads to the conclusion that the use of a 25mW LDV in this operation would be feasible.

REFERENCES

1. Coward, H. F., and Jones, G. W., "Limits of Flammability of Gases and Vapor", Bureau of Mines Bulletin 503 (1952).

2. Zabetakis, M. G., "Flammability Characteristics of Combustible Gases and Vapors", Bureau of Mines Bulletin 627 (1965).

3. Reuss, D. L., "Effect of Gravity on Lean Limit Flame Propagation", Ph.D. Thesis, Department of Aeronautical and Astronautical Engineering, University of Illinois at Urbana-Champaign (1979); also with R. A. Strehlow as Chapter III in Combustion Experiments in a Zero Gravity Laboratory, T. H. Cochran, Ed., Progress in Astronautics and Aeronautics, Vol. 73, pp. 61-89 (1981).

4. Levy, A. "An Optical Study of Flammability Limits", Proc. Roy. Soc., vol. 283,ser. A. p. 134 (1965).

5. Jones, G. W., and Kennedy, R. E., "Inflammability of Mixed Gases: Mixtures of Methane, Ethane, Hydrogen and Nitrogen", Bureau of Mines Report of Inv. #3172 (1932)

6. Von Lavante, E., "The Mechanism of Lean Limit Flame Extinction", Ph.D. Thesis, Department of Aeronautical and Astronautical Engineering, University of Illinois at Urbana-Champaign (1980); also with R. A. Strehlow, Combustion and Flame, 49, 123-140 (1983).

7. Meagher, G. M., "The Effect of Additives on the Ignition Delay Time for Stoichometric Propane-Air Mixtures", M.S. Thesis, Department of Aeronautical and Astronautical Engineering, University of Illinois at Urbana-Champaign (1978).

8. TSI Supplement, "Technical Data", Thermal Systems, Inc., St. Paul, MN (1981).

9. Adrian, R. J., and Fingerson, L. M., "The Dual Beam Laser Doppler Anenometer", A short course sponsored by Thermal Systems, Inc., St. Paul, MN (1976).

10. Meyers, J. F., Personal Communication, NASA Langley Research Center, Hampton, VA (1982)

APPENDIX A

```
      PROGRAM ABC (INPUT,OUTPUT)
      ALPH=10.8*3.14159/180.
      ANIT=3.14159/2.
      DO 10 I=1,26
      AI=I-1
      BETAU=ASIN(AI*SIN(ANIT+ALPH)/28.15)
      BETAL=ASIN(AI*SIN(ANIT-ALPH)/28.15)
      Y2U=28.15*SIN(BETAU+ALPH)
      X2U=28.15*COS(BETAU+ALPH)
      Y2L=28.15*SIN(BETAL-ALPH)
      X2L=28.15*COS(BETAL-ALPH)
      DELU=ASIN((1.0/1.49)*SIN(BETAU))
      DELL=ASIN((1.0/1.49)*SIN(BETAL))
      GAMU=ASIN(1.125*SIN(DELU))
      GAML=ASIN(1.125*SIN(DELL))
      EPU=GAMU-DELU
      EPL=GAML-DELL
      Y1U=25.36*SIN(BETAU+EPU+ALPH)
      X1U=25.36*COS(BETAU+EPU+ALPH)
      Y1L=25.36*SIN(BETAL+EPL-ALPH)
      X1L=25.36*COS(BETAL+EPL-ALPH)
      ETAU=ASIN(1.49*SIN(GAMU))
      ETAL=ASIN(1.49*SIN(GAML))
      ZETAU=BETAU+EPU-ETAU+ALPH
      ZETAL=BETAL+EPL-ETAL-ALPH
      X0=((Y1L-Y1U)+X1U*TAN(ZETAU)+X1L*TAN(-ZETAL))/
     *(TAN(ZETAU)+TAN(-ZETAL))
      Y0P=Y1L+(X1L-X0)*TAN(-ZETAL)
      DELX=-X0
      DELY=Y0P-AI
      ANG=(ZETAU-ZETAL)/2.0
      ANG=ANG*180./3.14159
      AROT=(ZETAU+ZETAL)/2.0
      AROT=AROT*180./3.14159
      PRINT 100,AI,Y0P,DELX,AROT,ANG
  100 FORMAT(5X,F5.1,4F10.3)
  110 FORMAT(5X,"ERROR")
   10 CONTINUE
      END
```

APPENDIX B

```
      PROGRAM ABC (INPUT,OUTPUT)
      CON=180./3.14159
      ANIT=3.14159/2.0
      ALPH=10.8*3.14159/180.
      Z2=28.15*TAN(ALPH)
      DEL=0.0645223
      Z1=Z2-3.175*TAN(DEL)
      Y2=0.0
      TH=0.0
      ZE=10.8
      YOP=0.0
      DX=25.36-(Z1/(TAN(ALPH)))
      PRINT 180,Y2,YOP,DX,TH,ZE
  180 FORMAT(5X,F5.1,3F10.3,F10.3)
      DO 10 I=1,25
      AI=I
      ALPH=10.8*3.14159/180.
      ALPH1=ASIN(AI/28.15)
      X2=28.15*COS(ALPH1)
      Y2=AI
      Z2=X2*TAN(ALPH)
      DO 10 J=1,2
      IF(J.EQ.2)ALPH=ZETA
      IF(J.EQ.2)ALPH1=THETA
      PRINT 150,ALPH,ALPH1,ZETA,THETA,Y2
      EL1=TAN(ALPH)
      EL2=TAN(ALPH1)
      EL3=SQRT(EL1**2+EL2**2)
      EL4=SQRT(1.0+EL1**2)
      EL5=SQRT(1.0+EL2**2)
      BETA=ACOS((EL4**2+EL5**2-EL3**2)/(2.0*EL4*EL5))
      IF(EL2.EQ.0.0)GAM=ANIT
      IF(EL2.EQ.0.0)GOTO 5
      GAM=ATAN(EL1/EL2)
    5 CONTINUE
      IF(J.EQ.1)DEL=ASIN((1.0/1.49)*SIN(BETA))
      IF(J.EQ.2)DEL=ASIN(1.49*SIN(BETA))
      AL=ALPH1*CON
      BE=BETA*CON
      GA=GAM*CON
      DE=DEL*CON
  110 FORMAT(5X,"ERROR")
  120 FORMAT(4F10.5)
      PRINT 140,EL1,EL2,EL3,EL4,BETA
  150 FORMAT(5E15.5)
      ARG=((EL4/EL3)*SIN(BETA))
      IF(ARG.GT.1.0)PRINT 130,AI
```

APPENDIX B (CONTINUED)

```
      IF(ARG.GT.1.0)OMEG=ANIT
      IF(ARG.GT.1.0)GOTO 15
  130 FORMAT(5X,"ARG GREATER THAN 1.0, AI=",I3)
      OMEG=ASIN(ARG)
   15 CONTINUE
      EPS=ANIT*2.0-DEL-OMEG
      EP=EPS*CON
      EL3P=EL5*(SIN(DEL)/SIN(EPS))
      EL2P=EL3P*EL2/EL3
      ETA=ALPH1-ATAN(EL2-EL2P)
      EL6=1.0/COS(ALPH1-ETA)
      EL1P=EL2P*TAN(GAM)
      ZETA=ATAN(EL1P/EL6)
      ET=ETA*CON
      ZE=ZETA*CON
      IF(J.EQ.2)GOTO 20
      THETA=ASIN(1.143*SIN(ETA))
      PRINT 160,ZETA,THETA
  160 FORMAT(2E15.5)
      ALPHP=ALPH1-ETA+THETA
      ALP=ALPHP*CON
      X1=25.36*COS(ALPHP)
      Y1=25.36*SIN(ALPHP)
      P=SQRT((X2-X1)**2+(Y2-Y1)**2)
      Z1=Z2-P*TAN(ZETA)
      OM=OMEG*CON
      TH=THETA*CON
      GOTO 10
   20 CONTINUE
      ALAMB=ALPHP-ETA
      ALA=ALAMB*CON
      X1P=Z1/(TAN(ZETA))
      DX=X1-X1P
      DY=X1P*TAN(ALAMB)
      Y0P=Y1-DY
      PRINT 150,EL1,EL2,EL3,EL4,EL5
      PRINT 150,X2,AL,BE,GA,DE
      PRINT 150,OM,EP,EL3P,EL2P,ET
      PRINT 150,EL6,EL1P,ZE,TH,ALP
      PRINT 150,X1,Y1,Z1,Y2,Z2
      PRINT 150,ALA,X1P,DX,DY,Y0P
      PRINT 180,Y2,Y0P,DX,ALA,ZE
      PRINT 100,AI,X1,X1P,Y1,Y1P,ALA,ZE
  140 FORMAT(4X,5F8.3)
   10 CONTINUE
  100 FORMAT(7F8.3)
      END
```

APPENDIX C

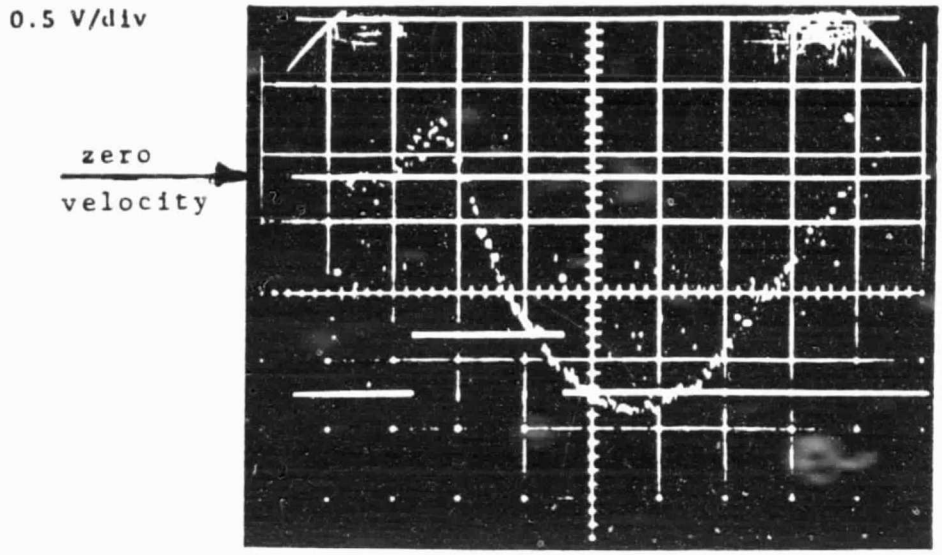

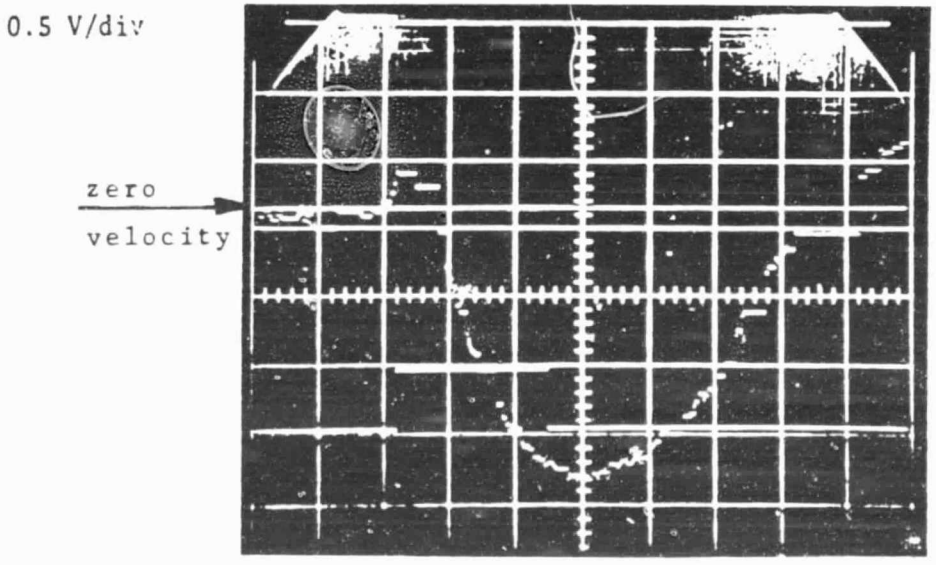

Figure C-1. Vertical velocity measurements at r = 0.

APPENDIX C (CONTINUED)

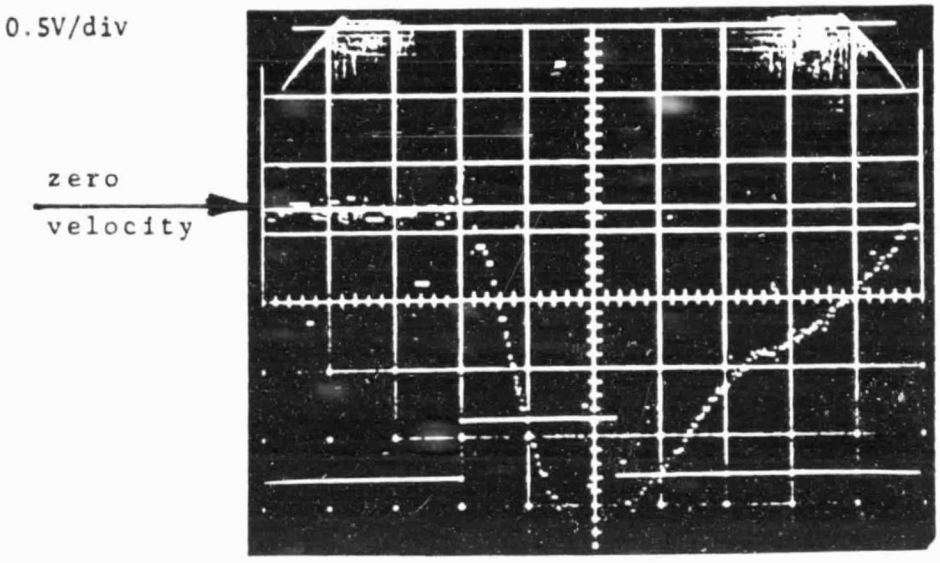

0.2 sec/div

Vertical velocity record

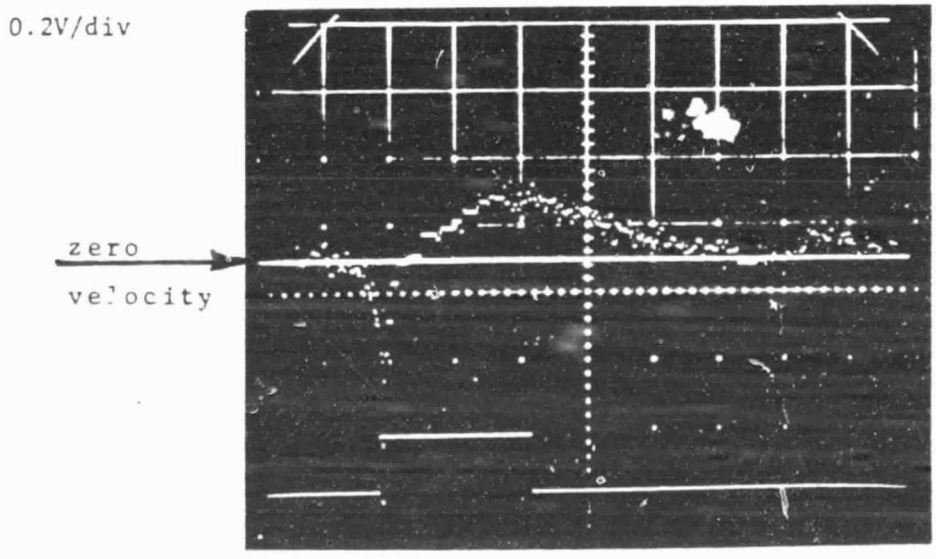

0.2 sec/div

Radial velocity record

Figure C-2. Velocity measurements at r = 5.0 mm.

APPENDIX C (CONTINUED)

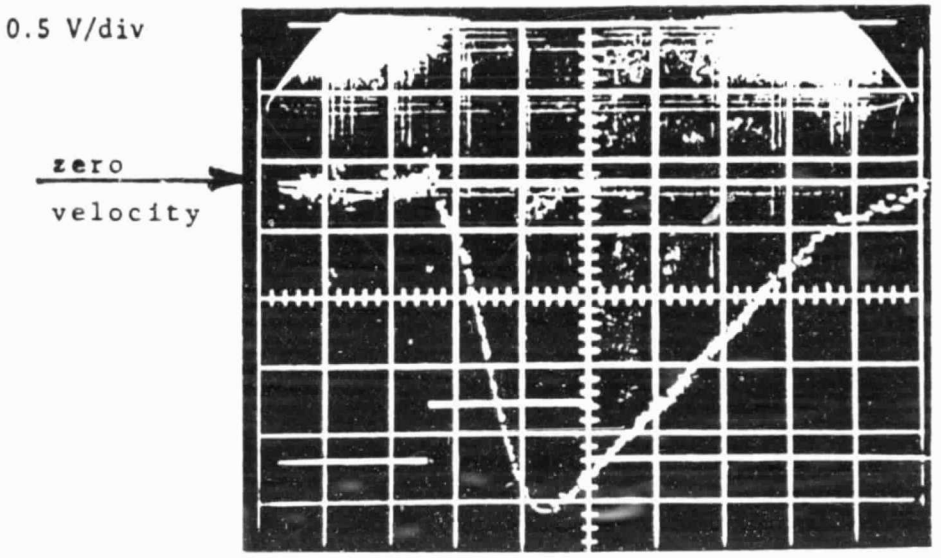

0.2 sec/div

Vertical velocity record

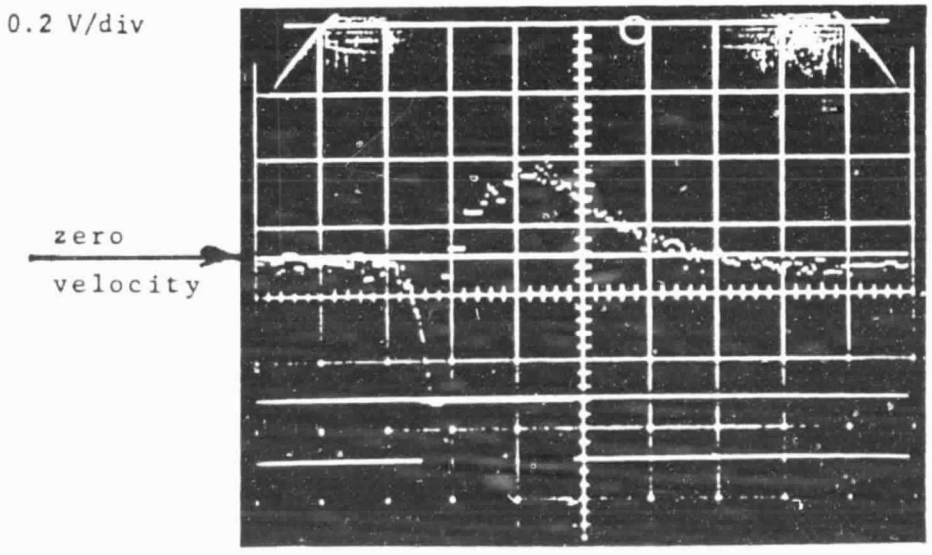

0.2 sec/div

Radial velocity record

Figure C-3. Velocity measurements at r = 10.0 mm.

APPENDIX C (CONTINUED)

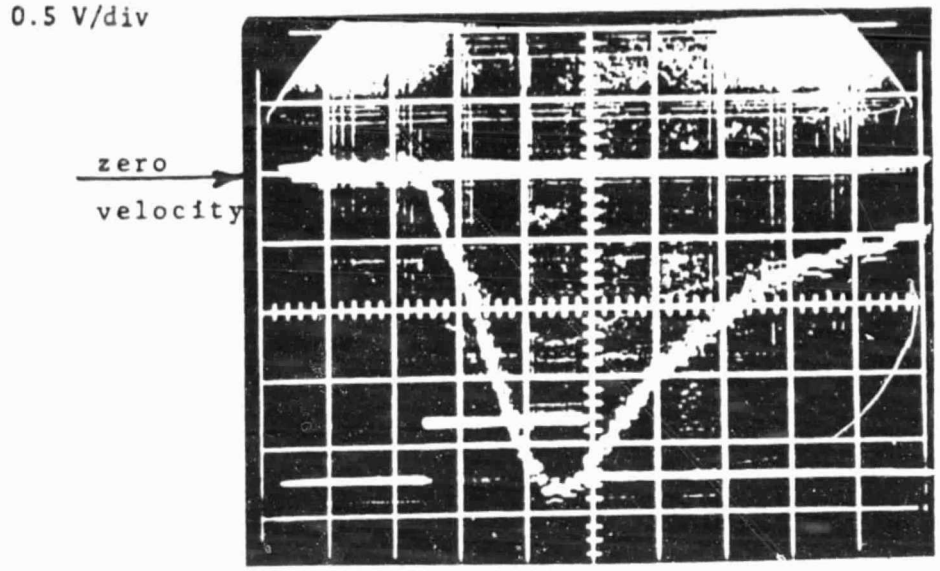

Vertical velocity record 0.2 sec/div

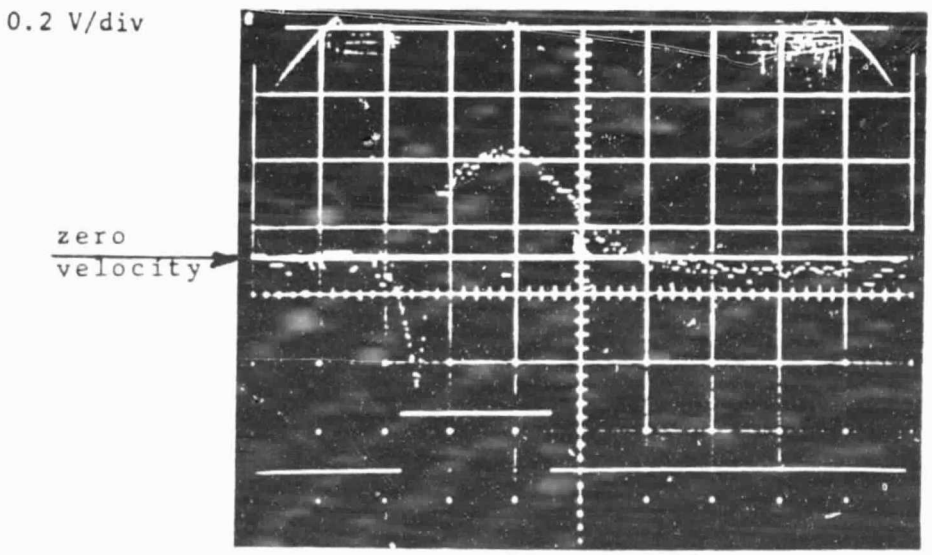

0.2 sec/div

Radial velocity record

Figure C-4. Velocity measurements at r = 15.0 mm.

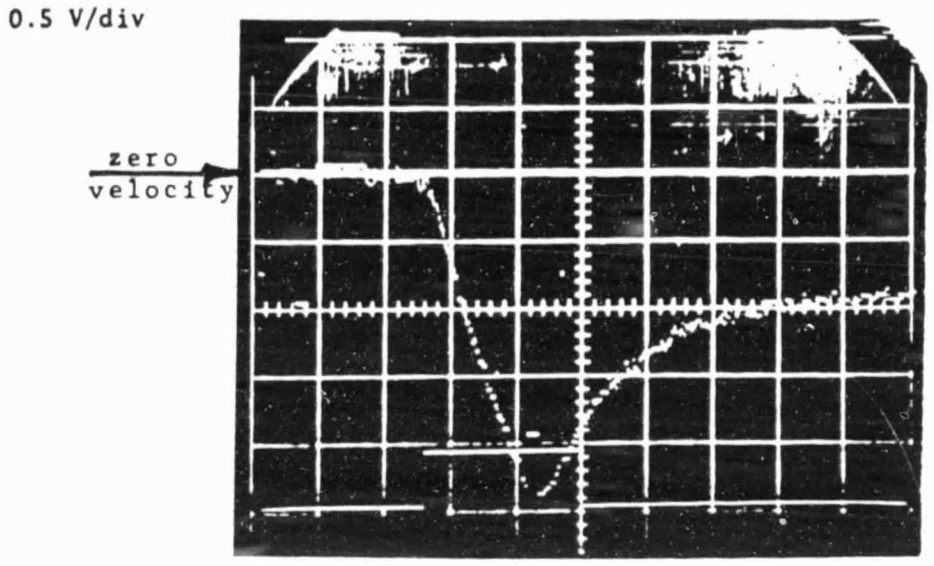

Vertical velocity record

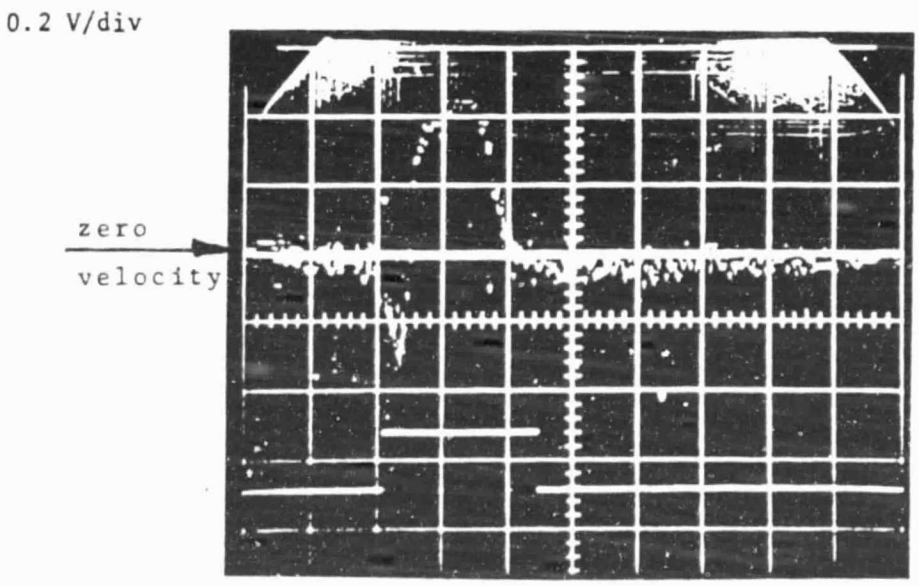

Radial velocity record

Figure C-5. Velocity measurements at r = 18.0 mm.

APPENDIX C (CONTINUED)

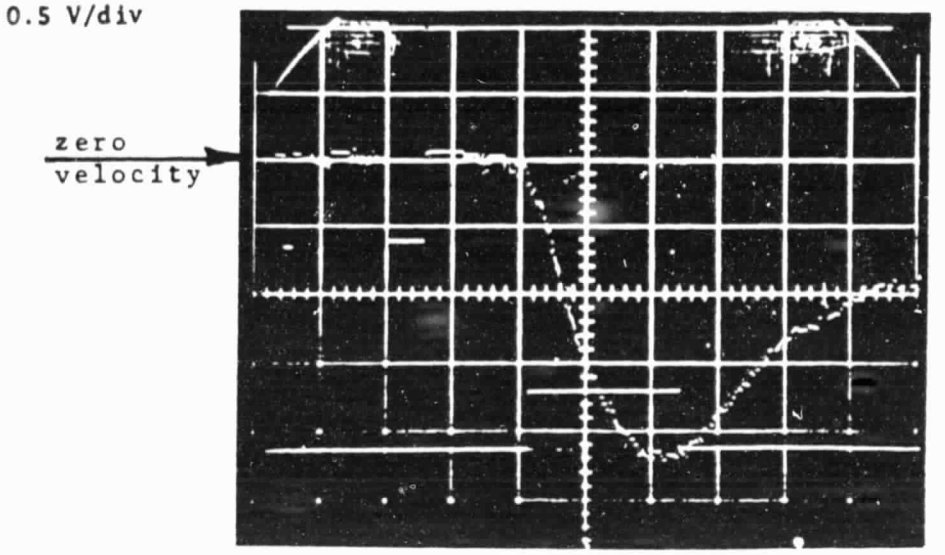

Vertical velocity record

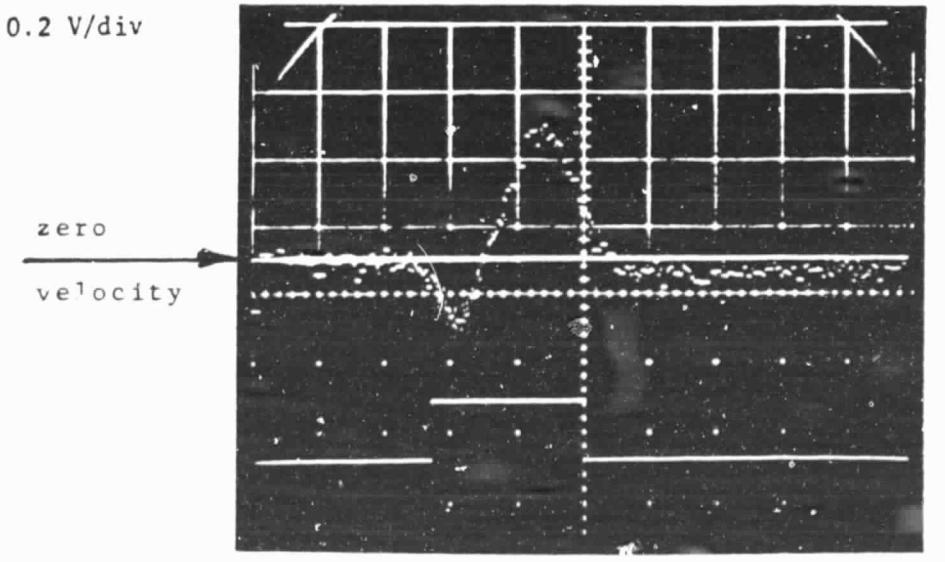

Radial velocity record

Figure C-6. Velocity measurements at r = 20.0 mm.

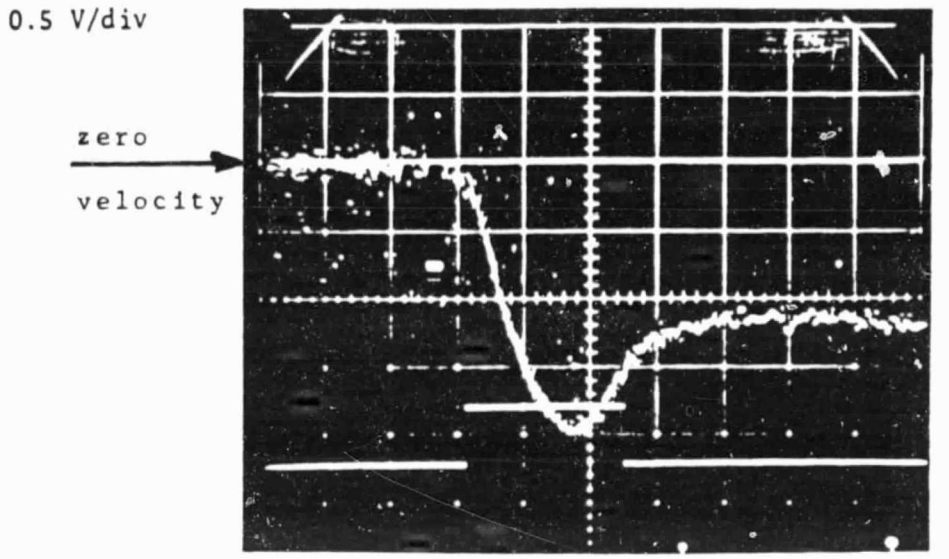

Vertical velocity record

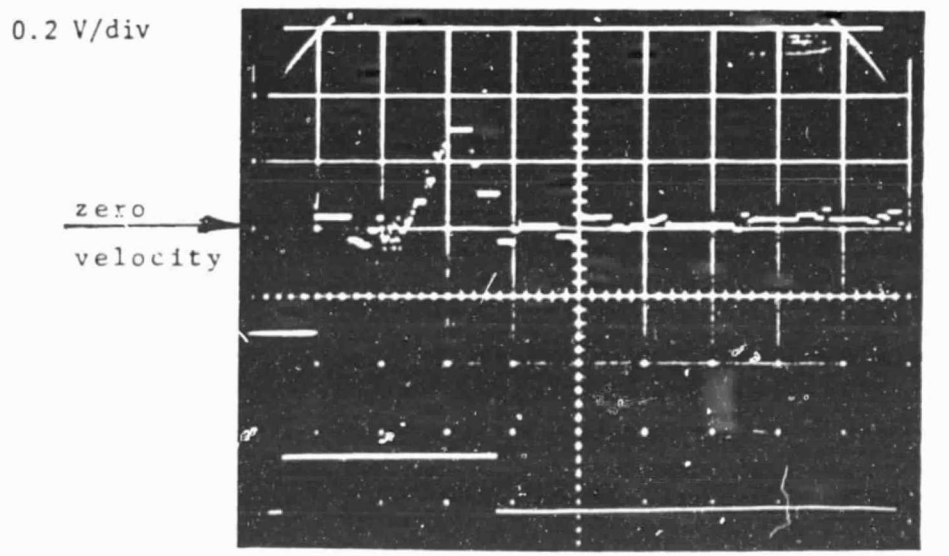

Radial velocity record

Figure C-7. Velocity measurements at r = 22.0 mm.

APPENDIX C (CONTINUED)

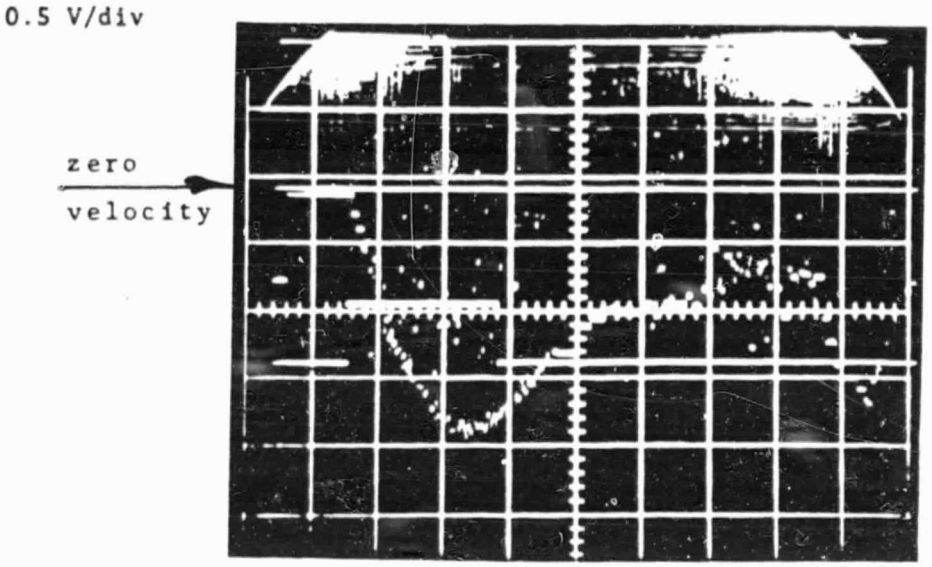

Vertical velocity record

Figure C-8. Velocity measurement at r = 23.5 mm.

RECENT AERONAUTICAL AND ASTRONAUTICAL ENGINEERING DEPARTMENT TECHNICAL REPORTS

Technical Report Number	Title	Author	Journal Publication
AAE 81-1 UILU ENG 81 0501	Shock Development and Transition to Detonation Initiated by Burning in Porous Propellant Beds	P. B. Butler H. Krier	
AAE 81-2 UILU ENG 81 0502	Development of a Single Species Equation of State for Determining Products Suitable for Hydrocode Calculations	L. H. Sentman R. A. Strehlow B. Haeffle A. Eckstein	
AAE 81-3 UILU ENG 81 0503	Large Deformation Dynamic Analysis of Laminated Plates by Finite Element Method	A. R. Zak	
AAE 81-4 UILU ENG 81 0504	Computer Programs for Automatic Input Data Generation for Finite Element Structural Codes ADINA and NASTRAN	A. R. Zak	
AAE 81-5 UILU ENG 81 0505	Nonlinear Interactions Between the Pumping Kinetics, Fluid Dynamics and Optical Resonator of cw Fluid Flow Lasers	L. H. Sentman M. H. Nayfeh	
AAE 81-6 UILU ENG 81 0506	An Algorithm for Minimum Weight Design of Structures Based on Optimality Criteria	W. Li	
AAE 81-7 UILU ENG 81 0507	Test and Evaluation of an Advanced Dynagun Ballistic Simulator	H. Krier D. W. Meeks	
AAE 81-8 UILU ENG 81 0508	A Theoretical and Experimental Study of cw HF Chemical Laser Performance	L. H. Sentman W. O. Mosebach	
AAE 82-1 UILU ENG 82 0501	A Subroutine for Calculating High Temperature CHONI Equilibrium	R. A. Strehlow	
AAE 82-2 UILU ENG 82 0502	Gaskinetics and Thermodynamic Aspects in Evaporation and Condensation Knudsen Layers	T. Ytrehus	

RECENT AERONAUTICAL AND ASTRONAUTICAL ENGINEERING DEPARTMENT TECHNICAL REPORTS (continued)

Technical Report Number	Title	Author	Journal Publication
AAE 83-1 UILU ENG 83 0501	MNORO3: An Efficient Rotational Nonequilibrium cw HF Chemical Laser Model	L. H. Sentman P. Schmidt	
AAE 83-2 UILU ENG 83 0502	Concepts of a General Substructuring System for Structural Dynamics Analyses	A. L. Hale L. V. Warren	
AAE 83-3 UILU ENG 83 0503	Approximate Modal Control of Distributed-Parameter Structures	A. L. Hale G. A. Rahn	
AAE 83-4 UILU ENG 83 0504	Users Guide for Program MNORO3	L. H. Sentman P. Schmidt	
AAE 83-5 UILU ENG 83 0505	Nonlinear Interactions Between the Pumping Kinetics, Fluid Dynamics and Optical Resonator of cw Fluid Flow Lasers	L. H. Sentman M. H. Nayfeh	
AAE 83-6 UILU ENG 83 0506	Effects of the HF Rate Package and the Optical Resonator on cw HF Chemical Laser Performance	L. H. Sentman P. F. Schmidt G. M. Marinos	
AAE 83-7 UILU ENG 83 0507	The Effects of Cavity Losses on the Performance of a Subsonic cw HF Chemical Laser	L. H. Sentman P. Renzoni S. Townsend M. H. Nayfeh K. K. King	
AAE 83-8 UILU ENG 83 0508	The Dynamic Synthesis of General Nonconservative Structures From Separately Identified Substructure Models	A. L. Hale L. A. Bergman	
AAE 83-9 UILU ENG 83 0509	Finite Element Model for Nonaxisymmetric Structure With Rate Dependent Yield Conditions	A. R. Zak	
AAE 83-10 UILU ENG 83 0510	Nonlinear Interactions Between the Pumping Kinetics, Fluid Dynamics and Optical Resonator of cw Fluid Flow Lasers	L. H. Sentman M. H. Nayfeh	

RECENT AERONAUTICAL AND ASTRONAUTICAL ENGINEERING DEPARTMENT TECHNICAL REPORTS (continued)

Technical Report Number	Title	Author	Journal Publication
AAE 84-1 UILU ENG 84 0501	Trailing Edge Flow Conditions as a Factor in Airfoil Design	A. I. Ormsbee M. D. Maughmer	
AAE 84-2 UILU ENG 84 0502	Time-Dependent Oscillations in a cw HF Chemical Laser Unstable Resonator	L. H. Sentman S. Townsend G. Tsioulos J. Bichanich M. H. Nayfeh K. K. King	
AAE 84-3 UILU ENG 84 0503	Stochastic Rotor Blade Dynamics	Y. K. Lin J. E. Prussing	
AAE 84-4 UILU ENG 84 0504	Sensing Angle of Attack	N. M. Karayanakis	
AAE 84-5 UILU ENG 84 0505	An Introduction to the Concept of Angle-of-Attack Feedback in Manual Control	N. M. Karayanakis	
AAE 84-6 UILU ENG 84 0506	Random Response of Turbine Structures Under Seismic Excitation	Y. K. Lin R. C. Y. Hong	
AAE 84-7 UILU ENG 84 0507	Finite Element Model for Gap Contact Problems	A. R. Zak	

RECENT AERONAUTICAL AND ASTRONAUTICAL ENGINEERING DEPARTMENT TECHNICAL REPORTS (continued)

Technical Report Number	Title	Author	Journal Publication
AAE 85-1 UILU ENG 85 0501	Low Thrust, Optimal, Time-free Transfer Between Coaxial, Aligned, Noncoplanar Elliptical Orbits	G. M. Marinos L. H. Sentman	
AAE 85-2 UILU ENG 85 0502	Behavior of the Lean Methane-Air Flame at Zero Gravity	K. A. Noe R. A. Strehlow	
AAE 85-3 UILU ENG 85 0503	An Experimental Study of Fabry-Perot and Stable Resonator cw HF Chemical Laser Performance	L. H. Sentman G. Tsioulos J. Bichanich D. Carroll	
AAE 85-4 UILU ENG 85 0504	The Use of a Laser Doppler Velocimeter in a Standard Flammability Tube	R. A. Strehlow E. M. Flynn	